

Experimental and Computational Demonstration of In Situ Pt Nanocluster-Decorated ZnO Film for Ultra-Sensitive Hydrogen Detection

Puja Ghosh, Pritam Ghosh, Rizwin Khanam, Chandra Shekhar Prajapati, Aarti Nagarajan, Shreeja Das, Rakesh Paleja, Sharan Shetty, Gopalakrishnan Sai Gautam, and Navakanta Bhat*



Cite This: <https://doi.org/10.1021/acsanm.5c04397>



Read Online

ACCESS |

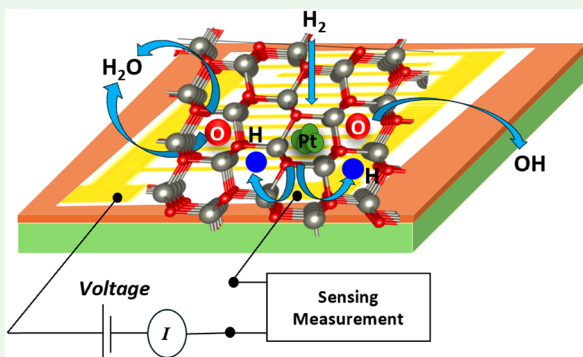
Metrics & More

Article Recommendations

Supporting Information

ABSTRACT: In this work, we present a Pt nanocluster-decorated ZnO thin film-based gas sensor for hydrogen detection, fabricated using the sputtering technique and in situ Pt decoration. The sensor exhibits a stable, highly sensitive, and repeatable response, making it a promising candidate for safety monitoring in hydrogen storage and transportation. Our sensor demonstrates optimal performance at an operating temperature of 225 °C with rapid response and recovery times (~10 and 3 s), high selectivity, and long-term stability. We deposit the ZnO thin film on an interdigitated electrode (IDE) substrate, with Pt added to the (002) polar plane by brief sputtering (1 to 6 s) to create an active sensing interface. We find that the Pt nanocluster-decorated ZnO sensor, with a deposition time of 2 s exhibits an enhanced response (~52,987%) to 1% hydrogen concentration, indicating its suitability for industrial applications. Our device demonstrates reliable detection of low hydrogen concentrations (~100 ppb), with a response of ~38% and no response drift over 1 year of testing, making it useful for environmental monitoring. To elucidate the role of Pt on ZnO for hydrogen sensing, we performed density functional theory calculations, analyzing adsorption and reaction energetics involving adsorbed H₂, O₂, O, OH, and H₂O, as well as lattice oxygen atoms on the ZnO (002) surface with and without Pt decoration. Our computational data is in agreement with experimental observations, identifying the oxygen-exposed (002) surface to be the most active for hydrogen sensing in both pristine and Pt nanocluster-decorated ZnO. Further, our computations highlight the role of Pt in enhancing hydrogen sensitivity via *i*) activating the autoreduction pathway of adsorbed hydroxide species, *ii*) spontaneous dissociation of adsorbed molecular hydrogen, and *iii*) keeping the lattice oxygen pathway of forming water active. Our systematic approach of designing sensors, combining a robust experimental setup with theoretical insights, is key in developing efficient hydrogen sensors, as well as in understanding the mechanisms behind such superior performance.

KEYWORDS: hydrogen, ZnO, Pt nanocluster, IDE, sputtering, DFT, stoichiometry, sensing mechanism



1. INTRODUCTION

The global interest to transition toward cleaner energy sources has positioned hydrogen as a pivotal component in the transition to sustainable energy systems.¹ Due to its high flammability in air, indicated by the low explosive limit (LEL) in volumetric terms of only 4%, reliable hydrogen leak detection is essential to ensure safety wherever hydrogen is produced or stored. A comprehensive discussion on the current overview of hydrogen sensing technologies and the evolving requirements of sensor performance for hydrogen systems can be found in the literature.² Current research efforts are focused on bridging the gap in designing fast, highly sensitive, and stable hydrogen sensing materials. Beyond its importance for safety monitoring, recent studies indicate that atmospheric hydrogen plays an indirect but significant role in climate processes. Although hydrogen is nontoxic, it can alter

the atmospheric oxidative capacity by consuming hydroxyl (OH) radicals, which can extend the lifetime of methane and contribute to tropospheric ozone.³ These conditions can potentially lead to global warming. Recent analysis shows that hydrogen possesses an indirect global warming potential.⁴ Hence, it is essential to develop hydrogen sensors capable of detecting trace-level concentrations for both safety assurance and accurate environmental monitoring.

Received: September 22, 2025

Revised: November 14, 2025

Accepted: November 18, 2025

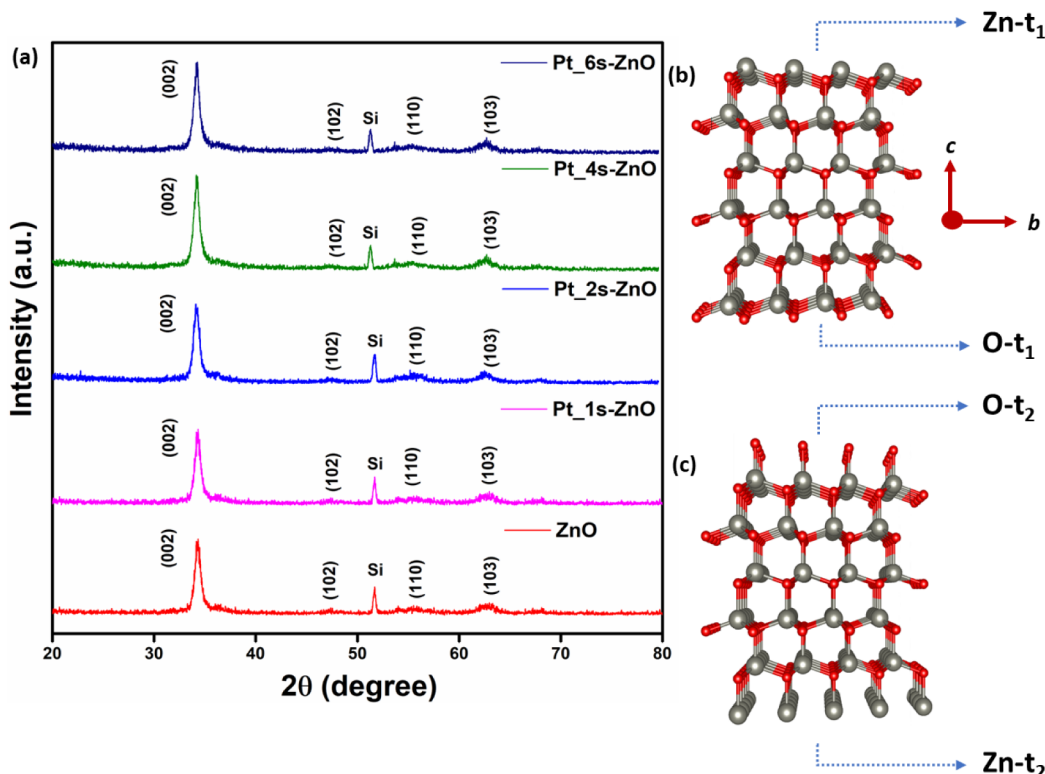


Figure 1. (a) XRD spectra of pure (red line) and Pt-decorated ZnO thin films on Si substrates. Pink, blue, green, and violet lines indicate Pt sputtered for 1, 2, 4, and 6 s on top of the ZnO, respectively. (b and c) Two possible terminations of the ZnO (002) surface, namely, t_1 (panel b) and t_2 (panel c). Red atoms are oxygen, gray atoms are zinc, and solid black lines are cell boundaries. Both terminations have sides that are filled with exposed Zn (labeled $Zn-t_1$ and $Zn-t_2$) and exposed O ($O-t_1$ and $O-t_2$) atoms.

Metal-oxide (MO_x) sensors have long been recognized for their versatility, cost-effectiveness, and adaptability in gas sensing, with applications in environmental monitoring of gases such as CH₄, NO₂, NH₃, CO, and CO₂. Metal oxides can undergo different surface reactions, like adsorption–desorption or oxidation–reduction, with target gases that lead to measurable changes in the sensor's electrical and physical properties.^{5–7} Among the extensively studied metal oxides, ZnO is a well-established material for practical sensing applications, owing to its wide bandgap, high surface area, chemical stability, affordability, and ease of synthesis.^{8–10} However, ZnO faces certain limitations, including response instability, low sensitivity, and poor selectivity, particularly toward hydrogen gas. To address these limitations, several enhancement strategies have been explored, such as noble metal doping (e.g., with Pd, Pt, Au, Ag, Sb, Co, and Cu) to modify ZnO's electronic properties and improve sensitivity and selectivity by enhancing surface reactivity and tuning charge transfer mechanisms.^{11–16} Additionally, surface functionalization has been applied to optimize defect states, such as oxygen vacancies, and to increase adsorption sites, which collectively enhance gas adsorption–desorption kinetics. These approaches have shown promise in improving the overall performance, selectivity, and long-term stability of ZnO-based gas sensors.

Previous studies on ZnO toward hydrogen sensing have often focused on optimizing material properties, differentiating the pure and doped material performance, and analyzing the effect of crystal size on sensor sensitivity, structural stability, and selectivity.^{17–20} For example, Rout et al.¹⁵ reported better sensing performance of ZnO nanowires and nanotubes,

synthesized by electrochemical deposition and doped with different molar concentrations of Pt, toward hydrogen. Phanichphant et al.²¹ produced 0.2–2.0 at. % Pt-doped ZnO by a single-step flame spray pyrolysis and reported successful hydrogen sensing. In another report, Tien et al.²² deposited Pt-coated ZnO nanorods using molecular beam epitaxy (MBE) and showed enhanced sensitivity toward hydrogen at 500 ppm levels with an N₂ background at room temperature. Also, Bhati et al.²³ deposited different wt % of Ni-doped (2, 4, and 6% Ni) ZnO nanostructures by radio frequency (RF) magnetron sputtering utilizing a Ni chip attached to a ZnO target and found the nanostructures to be highly sensitive toward low concentration levels of hydrogen. Some studies employed sputtering followed by postprocessing heat treatments to achieve hydrogen sensing at lower concentrations.^{24,25} Similarly, Hu et al. developed composite Pd-doped ZnO nanostructures with SnO₂,¹⁷ while Jiao et al. explored the on-chip growth of ZnO with PdO decoration via a chemical synthesis process.²⁶ Thus, studies so far indicate that ZnO's hydrogen sensing capabilities can be improved via surface decoration of noble metals (such as Pt and Pd), which can be attributed to the noble metals providing catalytic sites that enhance gas adsorption and charge transfer.^{19,21} Despite these advancements, the reported limit of detection (LOD) in the literature is above 100 ppm, and there remains a need for a scalable, reproducible, and cost-effective fabrication technique involving noble metal-decorated ZnO that can deliver stable and high-performance sensors. In this study, we present a simple *in situ* sputtering-based technique to fabricate ZnO thin films decorated with Pt, requiring minimal to no additional processing. Our cost-effective and scalable method produces

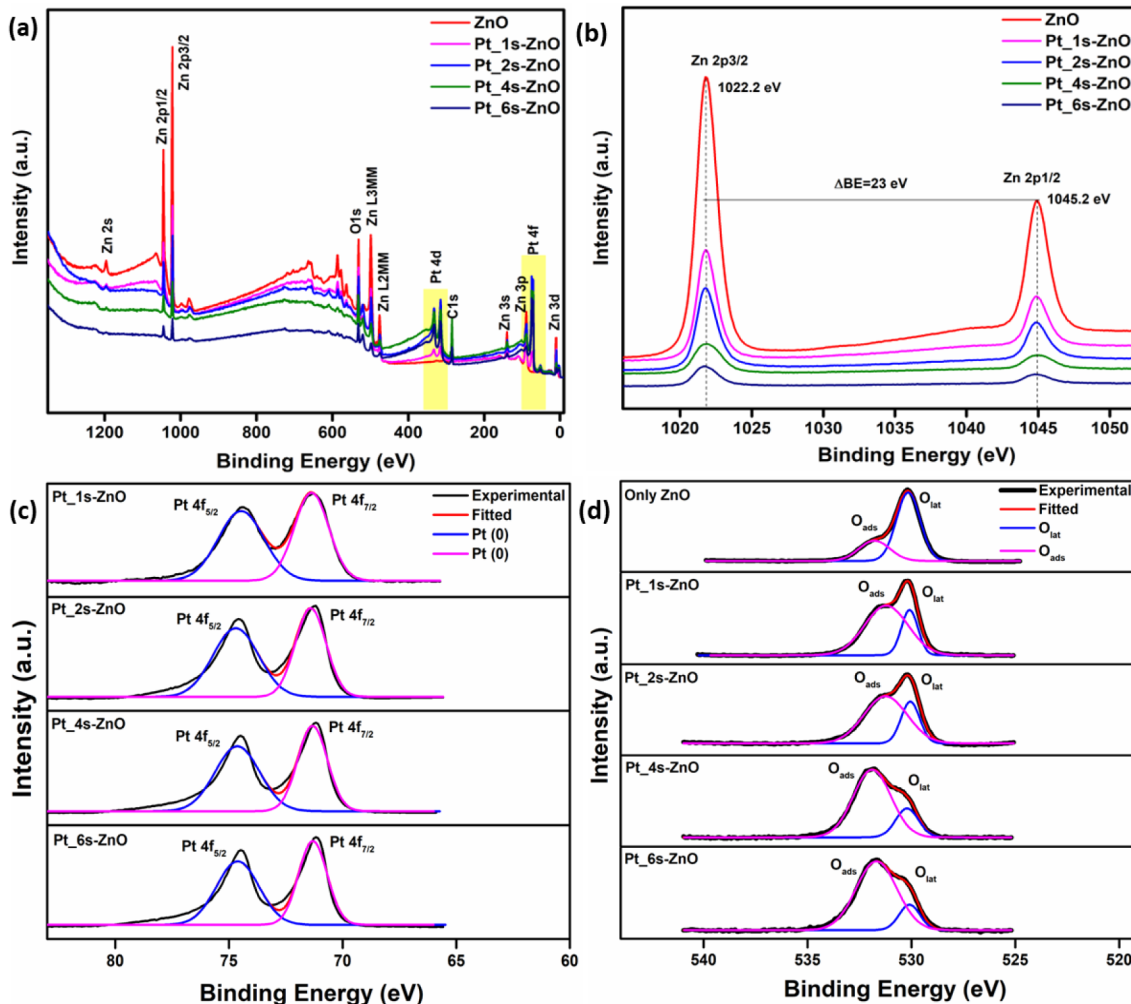


Figure 2. (a) Overall XPS spectra and (b) Zn 2p section of the XPS spectra in pristine (red) and Pt-decorated ZnO thin films, where pink, blue, green, and violet lines indicate Pt deposition times of 1, 2, 4, and 6 s, respectively. (c) Pt 4f and (d) O 1s core-level XPS spectra of ZnO thin films. While the Pt 4f spectra are displayed only for Pt-decorated samples, the O 1s spectra are shown for both pristine and Pt-decorated ZnO films.

robust and highly sensitive hydrogen sensors, addressing a significant challenge in hydrogen detection research. We also produce durable sensors with high sensitivity, and our thin films demonstrate good stability, maintaining consistent responses over one year without any signs of cracks or material degradation. To gain deeper insights into the sensing mechanism, we perform density functional theory (DFT)-based calculations, revealing the active role of the Pt nanocluster in the energetics of the hydrogen sensing process on polar ZnO surfaces. By exploring various surface reactions, we identified specific surface terminations and intermediate species that facilitate hydrogen sensing. Thus, our combined computational and experimental approaches offer a valuable framework that can be replicated in future gas sensor studies. Our findings highlight the effectiveness of our fabrication process, the fundamental mechanisms that drive sensor performance, and the pivotal role of noble metal decoration in optimizing MOx sensors for practical hydrogen leak detection and environmental monitoring.

2. RESULTS

2.1. Material Characterization. The crystal structure of both pristine and Pt nanocluster-decorated ZnO thin films (with Pt deposition times of 1, 2, 4, and 6 s) was analyzed by

using X-ray diffraction (XRD) in the range of 20° to 80°, as shown in Figure 1. All observed peaks align well with the standard JCPDS (Joint Committee on Powder Diffraction Standards) data No. #36–1451, confirming the hexagonal wurtzite structure of ZnO.²⁷ The diffraction peaks at approximately 34.30°, 47.72°, 55.58°, and 63.13° correspond to the (002), (102), (110), and (103) crystallographic planes, respectively, which are characteristic of wurtzite ZnO.²⁸ The films demonstrate a strong preferential orientation along the (002) plane, indicating that the ZnO nanostructures grow anisotropically along the *c*-axis. The growth along the *c*-axis is particularly beneficial for gas sensing applications, as it typically enhances surface accessibility and the density of active sites available for gas adsorption.²⁹ The increased peak intensity along the (002) plane further suggests high crystalline quality, which is advantageous for consistent electron transport and response stability in gas sensing. No Pt-related diffraction peaks are detected in the Pt-decorated ZnO films due to the minimal Pt content, which does not form distinct crystalline phases detectable by XRD. The crystallite size of the ZnO films was calculated from the XRD data and is discussed in Table S1.

The (002) surface of ZnO, which we observe to be the preferred direction of growth from our XRD measurements (Figure 1a), is a polar surface that can have two possible

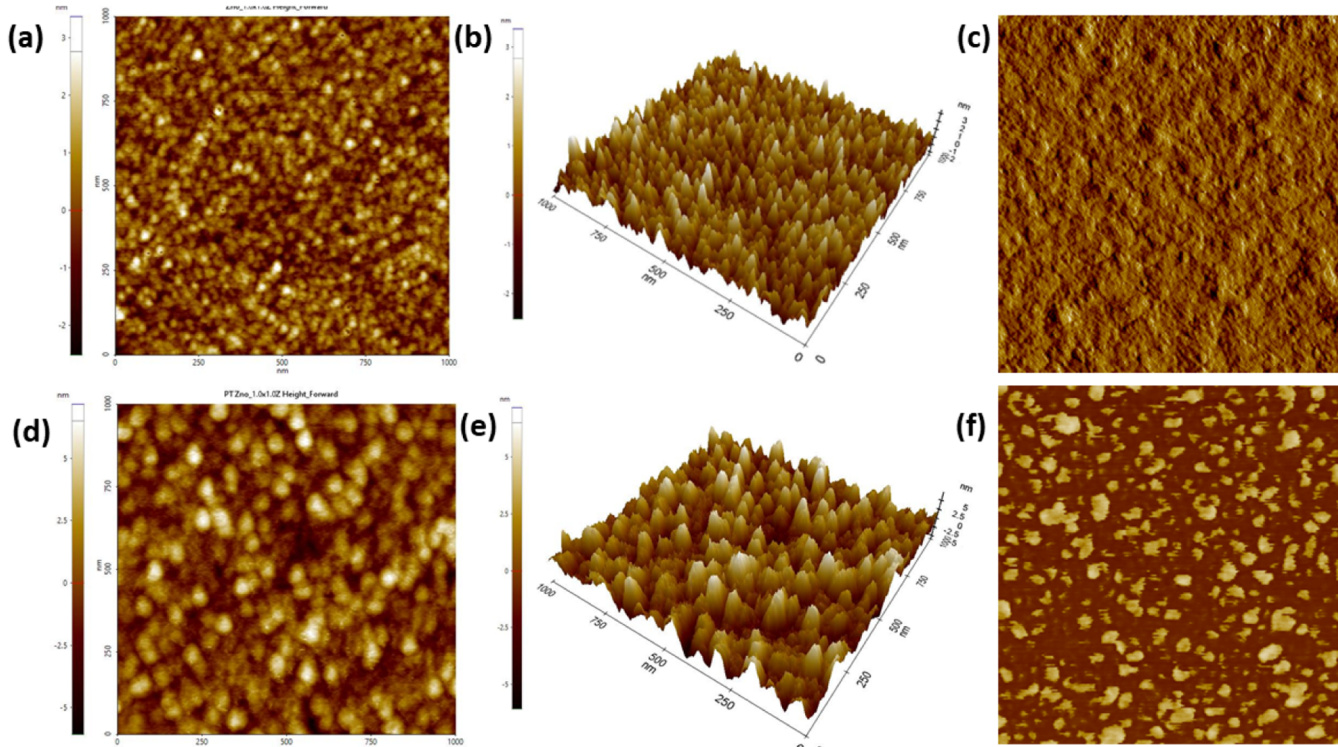


Figure 3. (a, d) 2D, (b, e) 3D, and (c, f) phase difference images obtained from AFM of pristine (top row) and Pt-decorated (bottom row) ZnO thin films. We performed AFM measurements on the Pt-decorated sample with 2 s of Pt deposition.

terminations, each with exposed Zn and O atoms, as shown in Figure 1b,c, i.e., the t_1 termination with exposed Zn and O (Zn- t_1 and O- t_1 , Figure 1b) and the t_2 termination with exposed Zn and O (Zn- t_2 and O- t_2 , Figure 1c). Multiple studies on ZnO-based sensors have indicated the polar planes (001) and (002) to be the dominant plane(s) upon synthesis and have been considered to contribute heavily to the sensing performance via the presence of active sites.^{30–34} We employed DFT to calculate the absolute surface energies of both terminations of the (002) plane to determine the ground-state configuration (see Table S7 and Section S5 for details). Since both terminations of the (002) surface are polar with a net dipole moment perpendicular to the surface along the c -axis, we capped one side of the surface with pseudohydrogen atoms (see Figure S5 and Table S6)^{35–37} and used the nonpolar (100) ZnO surface as a reference surface to compute absolute surface energies. The surface energies of the O- t_1 (Zn- t_1) and the O- t_2 (Zn- t_2) surfaces exhibit surface energies of 1.84 (1.90) and 9.57 (5.83) J/m², respectively, indicating that the t_1 termination is thermodynamically favored to form. Thus, we expect one of the t_1 terminations to form primarily during sputtering and use both Zn- and O-exposed facets of the t_1 termination to perform further DFT calculations.

We employed scanning electron microscopy (SEM) to investigate the surface morphology and structural integrity of pristine and Pt nanocluster-decorated ZnO thin films. Panels a–e in Figure S1 illustrate that the films exhibit a smooth, wrinkle-free surface without any visible cracks, even after Pt decoration. Such uniform distribution across the substrate suggests high-quality thin-film deposition with minimal defects, which is essential for reliable sensor performance. Cross-sectional SEM imaging reveals a progressive increase in film thickness corresponding to increased Pt deposition time. For

example, the thickness for pristine ZnO is measured at 39.8 nm (Figure S1a), while the thickness for Pt nanocluster-decorated ZnO is around 40, 40.2, 41.4, and 43.2 nm for 1, 2, 4, and 6 s of Pt deposition, respectively (Figure S1b–e). Thus, our in situ process with controlled Pt deposition allows for precise tuning of the film's sensing properties, unlike chemical techniques. Figure S1f shows SEM imaging of the interdigitated electrodes (IDE), where Pt-decorated ZnO particles are evenly distributed, confirming the homogeneity of the sputtering deposition process. This homogeneity is crucial in sensing devices, as it ensures that the entire sensing region of the IDE is covered with active material, allowing for a consistent response when exposed to target analytes.

Electron probe microanalysis (EPMA) was conducted to examine the elemental distribution within pristine and Pt nanocluster-decorated ZnO thin films. Figure S2 provides an elemental map of Pt-decorated ZnO (at a deposition time of 2 s), highlighting the distribution of Si, Zn, O, and Pt across the IDEs. We performed EPMA point analysis for Pt deposition times of 1, 2, 4, and 6 s and summarized the results in Table S2. Importantly, we observe a progressive increase in Pt content as deposition time is extended, ranging from 1.30 to 14.62 mass% Pt from 1 to 6 s deposition time, indicating a gradual enhancement of Pt coverage on the ZnO surface.

To get a deeper understanding of the chemical oxidation states and elemental composition of the thin films, we performed X-ray photoelectron spectroscopy (XPS) on all of the fabricated ZnO films. As shown in Figure 2a, Zn and O are present in the pristine ZnO film, and an additional peak corresponding to Pt is observed in the Pt nanocluster-decorated ZnO films (highlighted in yellow). No additional peaks for other impurities were detected, confirming the high purity of the fabricated samples. For both pristine and Pt

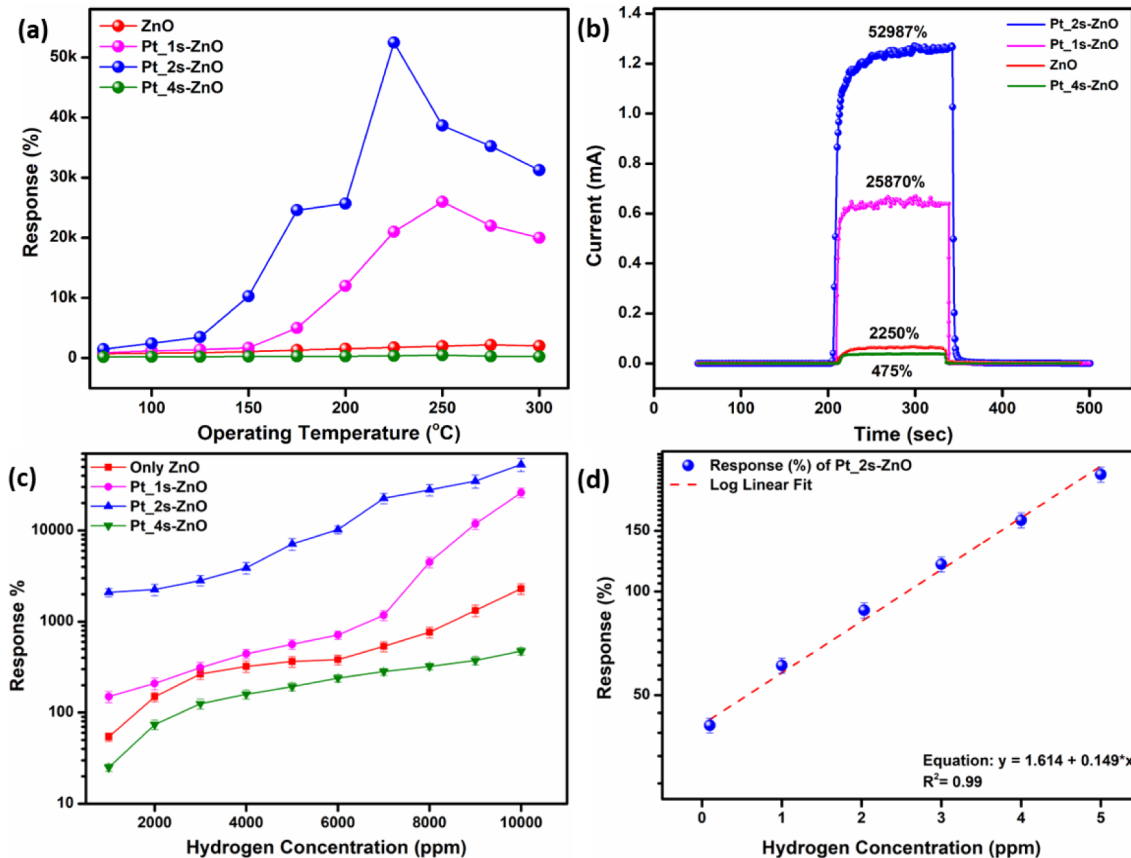


Figure 4. (a) Response (%) variation with operating temperature ranging from 25 to 300 °C at 10k ppm of hydrogen gas, (b) response (measured in current) as a function of time when 10k ppm of hydrogen gas is introduced, and (c) response at different hydrogen concentration levels for pristine and Pt-decorated ZnO thin film sensors. Red, pink, blue, and green symbols and lines in panels a, b, and c represent pristine, 1 s, 2 s, and 4 s Pt-deposited ZnO samples. (d) Linearity in the response of the sensor as a function of hydrogen concentration at low ppm levels.

nanocluster-decorated ZnO films, the XPS spectra exhibit two prominent peaks at binding energies of 1045.2 and 1022.2 eV, which correspond to the Zn 2p_{1/2} and Zn 2p_{3/2} levels, respectively.³⁸ These peaks are characteristic of the +2 oxidation state of zinc (Zn^{2+}) that is expected within the ZnO structure, as shown in Figure 2b. The core-level XPS spectra of Pt 4f in Pt-decorated ZnO films, presented in Figure 2c, highlight two distinct doublet peaks across all samples, which we identify as Pt 4f_{7/2} and Pt 4f_{5/2} at binding energies of 70.8 and 74.8 eV, respectively. Both peaks correspond to the Pt⁰ oxidation state, which indicates metallic Pt. The O 1s core-level spectra in Pt-decorated ZnO films, shown in Figure 2d, exhibit two primary components: lattice oxygen species (O_{lat}) at ~530.5 eV and adsorbed oxygen species (O_{ads}) at ~531.5 eV. The relative amounts of both O_{lat} and O_{ads} are calculated and presented in Table S3. Notably, the Pt nanocluster-decorated ZnO films have a higher relative percentage of O_{ads} compared to pristine ZnO, where the O_{ads} can contribute better to gas sensing than O_{lat} .^{39,40} In summary, the XPS data indicate the presence of both metallic Pt and a higher amount of O_{ads} , which can act in a combined manner and give rise to a better hydrogen sensing response.

For analyzing the surface roughness and topological characteristics of the ZnO thin films, we used atomic force microscopy (AFM). Particularly, we investigated the change in the root-mean-square (RMS) roughness to understand the effect of surface roughness on gas sensing performance. AFM images in both two-dimensional (2D) and three-dimensional

(3D) views across a 1 μ m scanning area, as displayed in Figure 3, demonstrate a uniform film coverage across the substrate. The quantitative analysis reveals that surface roughness increases with increasing Pt deposition time, with RMS values measured at ~0.79 nm for pristine ZnO and subsequently increasing to 1.23, 1.98, 2.15, and 2.69 nm for ZnO films decorated with Pt for 1, 2, 4, and 6 s, respectively. The progressive roughening of the surface due to Pt nanocluster decoration is visible in the AFM images (see panels b and e of Figure 3). The ZnO surface layer becomes increasingly textured compared to the smooth surface of pristine ZnO, possibly allowing for more sites for hydrogen chemisorption in the Pt nanocluster-decorated sample.^{41,42} The higher roughness can also facilitate the adsorption of oxygen species, which may be crucial for hydrogen sensing. The AFM data also show a clear phase difference between the pristine and Pt-decorated ZnO thin films (panels c and f of Figure 3), which highlights the topological changes caused by Pt nanocluster decoration.

We conducted temperature-dependent current–voltage (I – V) measurements across a –1 V to +1 V range to evaluate the suitability of the IDEs for hydrogen sensing (see Figure S3). The devices based on pristine ZnO and Pt nanocluster-decorated ZnO with deposition times of 1, 2, and 4 s display typical semiconducting behavior between 25 and 200 °C, with an increase in current as a function of increasing temperature, which is desirable for gas sensing. In contrast, the ZnO device with 6 s of Pt deposition exhibits a decrease in current with increasing temperature, which signifies metallic behavior. Thus,

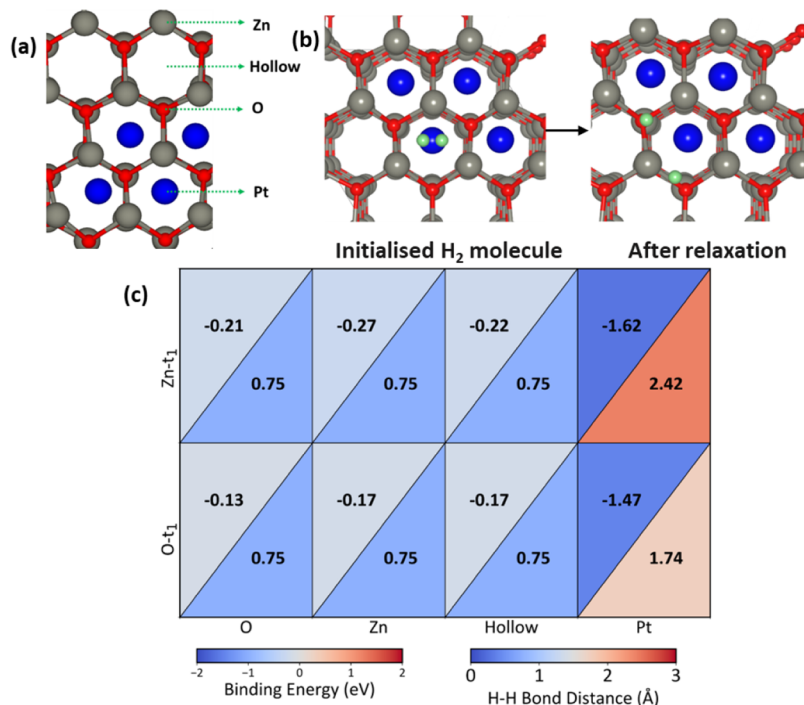


Figure 5. (a) Top view of four adsorption sites considered for possible H₂ adsorption is illustrated on a Zn-t₁ ZnO surface that is decorated with a Pt₄ cluster. (b) Demonstration of facile dissociation of an H₂ molecule on the Pt cluster upon structure relaxation. Blue, gray, red, and green spheres as Pt, Zn, O, and H, respectively. (c) H₂ binding energies (in eV, upper triangles) and H–H bond distances (in Å, lower triangles) postadsorption for various initializations (on O, on Zn, hollow, and on Pt sites) on the Zn-t₁ (upper row) and O-t₁ (lower row) surfaces of ZnO.

the excessive Pt content in the 6 s sample creates a conductive path for electrons that overrides the underlying semiconducting response of ZnO, reducing the sensitivity of the sample to any interactions with gas molecules and making the sample unsuitable for sensing (Figure S3). Therefore, we select pristine and Pt nanocluster-decorated ZnO (with 1, 2, and 4 s of Pt deposition) for further hydrogen sensing experiments.

2.2. Gas Sensing Response. To evaluate the gas sensing performance, we exposed all fabricated sensors to hydrogen gas (of different concentrations) at varying operating temperatures, ranging from 25 to 300 °C. The sensing response of the material toward different hydrogen concentrations is quantified as a response (in %) using eq 1, where I_g and I_a correspond to the measured current in the presence of hydrogen gas and synthetic air, respectively.

$$\text{Response}(\%) = \frac{I_g - I_a}{I_a} \times 100\% \quad (1)$$

Figure 4a plots the response of pristine ZnO (red lines and symbols) and Pt-decorated ZnO with 1 s (pink), 2 s (blue), and 4 s (green) Pt deposition times as a function of operating temperature. Notably, pristine ZnO exhibits its highest response at 275 °C, while the Pt nanocluster-decorated sensors achieve their maximum response at 225 °C. Typically, sensors exhibit an optimal operating temperature that is determined by the trade-off between the spontaneity of gas species adsorption on the surface and any activation energies that the system has to overcome to facilitate a chemical reaction (or a change in material property). Importantly, Pt nanocluster-decorated samples (with 1 and 2 s deposition times) display significantly higher responses (~11.5 and 23.5 times higher than pristine ZnO), highlighting the effectiveness of the Pt decoration over ZnO in hydrogen sensing. Given that

Pt nanocluster-decorated samples exhibit their highest response at ~225 °C, we select this as the optimal temperature for further sensing measurements.

Figure 4b displays the response (plotted as measured current) of pristine and Pt nanocluster-decorated ZnO-based sensors as a function of exposure time to 10 000 ppm of hydrogen gas, operated at their optimal operating temperature with an exposure time of 3 min. Importantly, on the Pt nanocluster-decorated ZnO sensor (with 2 s deposition time), the response to hydrogen gas reaches 52,987%, which is significantly higher than other samples, including the 1 s Pt-deposited ZnO (25,870%), 4 s Pt-deposited ZnO (475%), and pristine ZnO (2,250%). All the sensors demonstrate reversibility upon switching the hydrogen gas to the baseline dry air. The presence of Pt nanoclusters on ZnO modifies the electronic properties of ZnO to amplify the sensor's response by facilitating electron exchange with hydrogen. However, the reduction in response at higher degrees of Pt coverage (as obtained with the 4 s Pt-deposited ZnO sensor) is possibly due to an increased metallic character of the surface that suppresses the underlying semiconducting nature of ZnO, and possibly excessive coverage of the active sites on ZnO by Pt nanoclusters.

In our response measurements (panels a and b of Figure 4), we find the optimal Pt nanocluster deposition time to be 2 s on the pristine ZnO surface, which is able to balance the increased interactions with hydrogen gas without adversely affecting the semiconducting nature of ZnO. Indeed, we find the 2 s Pt-deposited sample to show the best response among other samples operating at 225 °C across a range of hydrogen concentrations (i.e., from 1000 to 10k ppm), as shown in Figure 4c. The linearity in the response of the sensor as a function of higher concentrations (1000 to 10k ppm) of

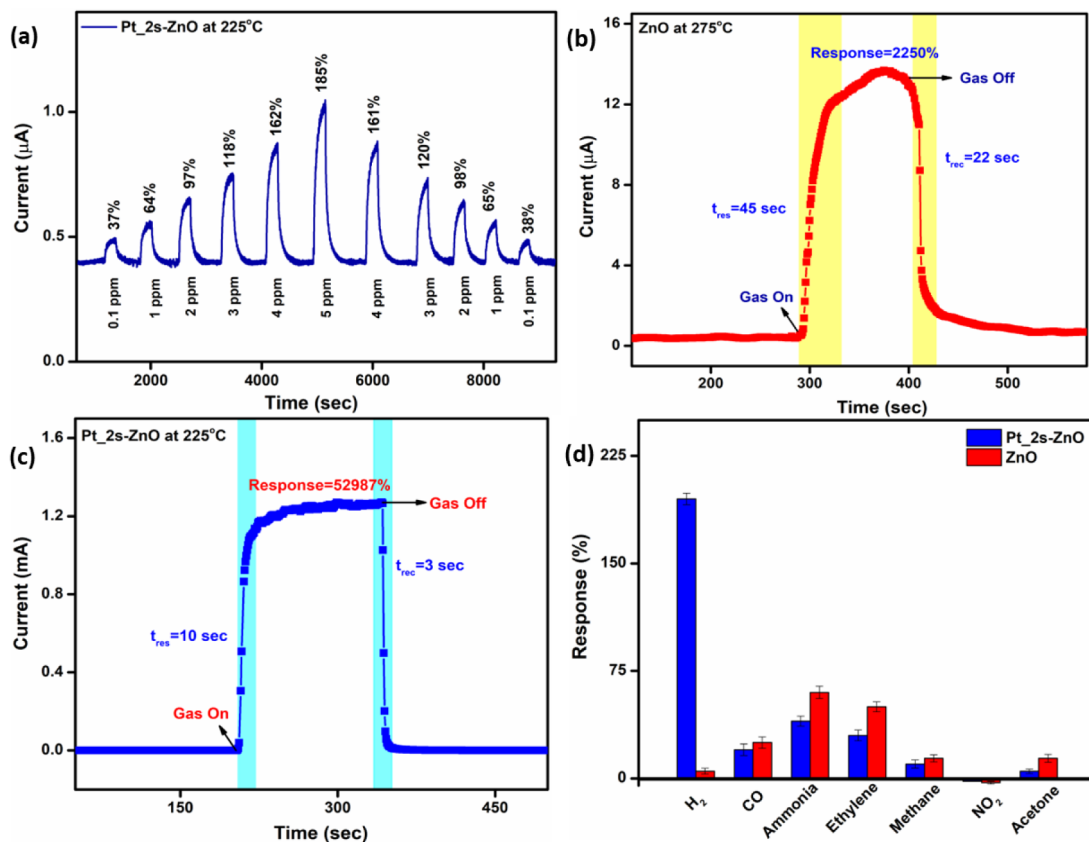


Figure 6. (a) Dynamical response of Pt nanocluster-decorated ZnO (2 s deposition time, 225 °C operating temperature) at low hydrogen concentrations ranging from 0.1 to 5 ppm. (b and c) Response and recovery time quantification at 10k ppm hydrogen concentration, as highlighted by the yellow and blue highlighted regions, for (b) pristine and (c) Pt-decorated (2 s deposition time) ZnO sensor, operating at 275 and 225 °C, respectively. (d) Selectivity of pristine (red bars) and Pt-decorated (blue, 2 s deposition time) ZnO sensors toward different gases.

hydrogen is shown in Figure S4b. The sensor exhibits a linearly varying response (dotted red line shown in Figure 4d) at low hydrogen concentrations (i.e., from 0.1 to 5 ppm), which simplifies calibration of the device in practical applications.

To understand the differences in sensing response between the pristine and Pt nanocluster-decorated ZnO, we investigated H₂ adsorption on both surfaces using DFT. We primarily used binding energies (E_{binding}), as defined in eq 2, to examine the spontaneity of adsorption of any species over the ZnO surface. $E_{\text{slab} + \text{adsorbate}}$, E_{slab} , and $E_{\text{adsorbate}}$ indicate the DFT-calculated total energies of the slab model along with an adsorbate, the pristine slab model, and the isolated adsorbate, respectively. The adsorbate here can be a molecule or a cluster of Pt atoms on the ZnO surface. In general, negative binding energies indicate strong spontaneous adsorption of a species on a slab (or substrate).

$$E_{\text{binding}} = E_{\text{slab} + \text{molecule}} - E_{\text{slab}} - E_{\text{molecule}} \quad (2)$$

Given that Pt decoration plays a crucial role in sensor performance, we placed a four-atom Pt cluster (or Pt₄ cluster) on the pristine ZnO surface to capture the effect of Pt. Although larger Pt clusters are generally more stable,^{43,44} we considered a “small” cluster in our work to capture the effect of Pt at a reduced computational cost. We calculated binding energies for the planar and tetrahedral geometries of the Pt₄ cluster (i.e., the adsorbate in eq 2 is a Pt₄ cluster), initialized on different sites on both the O-t₁ and Zn-t₁ surfaces, with the low-energy relaxed geometries displayed in Figure S6 and the

lowest energies compiled in Table S8. Importantly, we find the planar Pt₄ geometry to be the stable configuration on both the O-t₁ and Zn-t₁ surfaces and subsequently use this configuration for further H₂ adsorption calculations (see below).

For modeling H₂ adsorption on the pristine and Pt nanocluster-decorated ZnO surface, we considered four distinct surface sites: Zn, O, hollow, and Pt, as shown in Figure 5a. Note that the on-Pt site is the “point of difference” between the pristine and Pt-decorated ZnO surfaces. We have analyzed the nearby O, Zn, and hollow sites in the presence of Pt decoration, and we observe no activation of neighboring sites in the presence of the Pt nanocluster (see Figure S8 and Table S9); hence, those are not considered for further analysis. We consider the on-Pt site to be the only additional site that is available upon Pt decoration, while the three remaining sites are already available for H₂ adsorption in pristine ZnO. Thus, any changes that Pt decoration can effect on ZnO, with respect to H₂ adsorption, will be captured by the binding energy exhibited by the on-Pt site compared to the three remaining sites.

The binding energies for H₂ adsorption on each of the four sites on the O-t₁ and Zn-t₁ surfaces are presented as a heat map in Figure 5c, where the upper triangle within each cell represents the corresponding binding energy. While considering H₂ adsorption on a Pt-decorated cluster, we refer to the H₂ molecule as the adsorbate in eq 2 and the ZnO surface, including the Pt₄ cluster, as the slab. The lower triangles in each cell of Figure 5c indicate the H–H bond distance postadsorption (i.e., upon structure relaxation). We observe

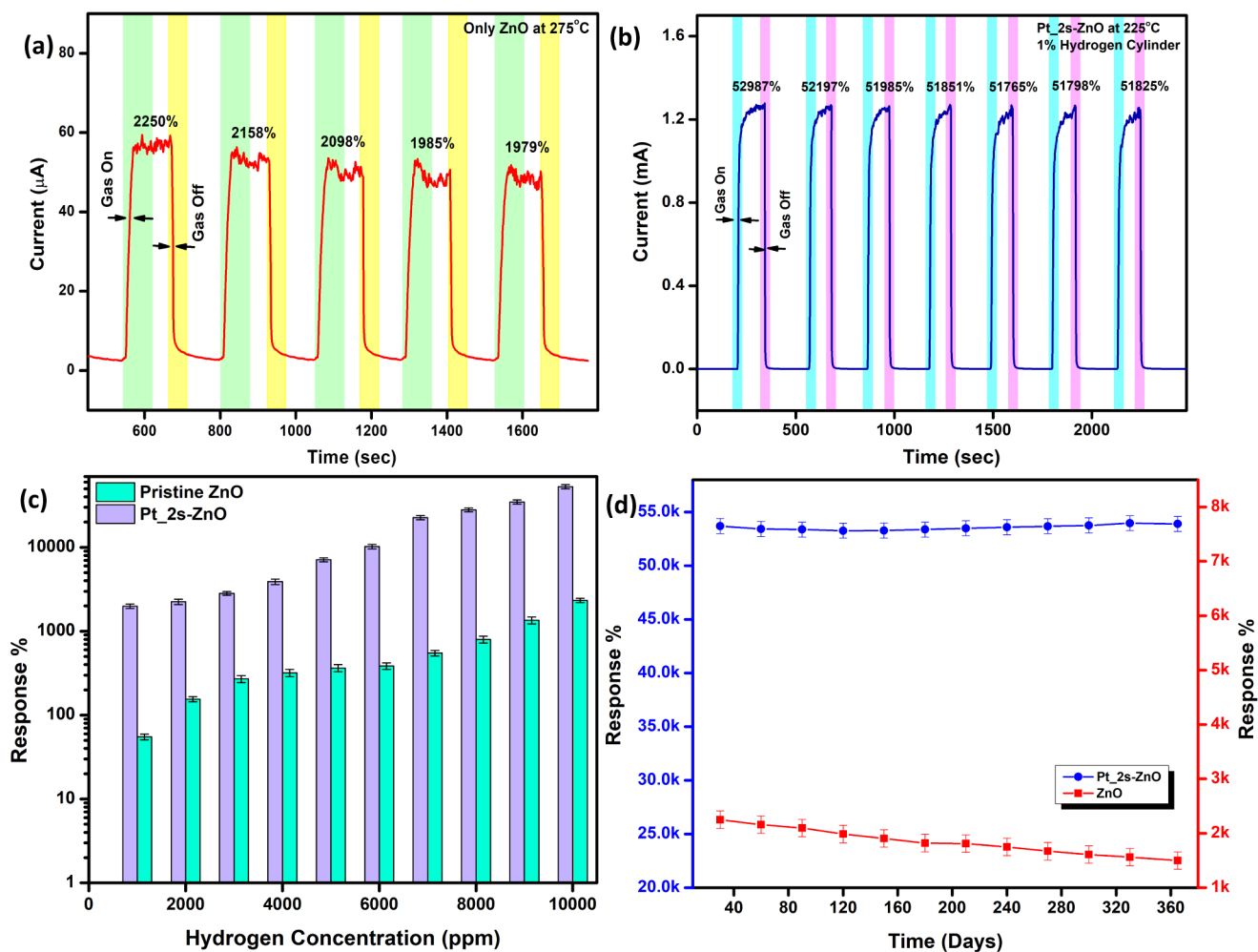


Figure 7. Repeatability in response over multiple cycles of 1% hydrogen exposure for (a) pristine and (b) Pt-decorated (2 s deposition time) ZnO, operating at 275 and 225 °C, respectively. (c) The average response % over three samples as a function of hydrogen concentration, with the error bars representing the standard deviations. (d) Long-term stability in sensor response of the pristine ZnO (red symbols) and Pt-decorated ZnO (2 s deposition time, blue symbols) devices with time after fabrication.

that H₂ binds quite weakly, i.e., without significant dissociation of the H₂ molecule, on pristine ZnO surfaces. For example, the H₂ binding energies on both O-t₁ and Zn-t₁ range from -0.13 to -0.22 eV across the on O, on Zn, and hollow sites (Figure 5c), with the H₂ bond distances postadsorption (~0.75 Å) quite similar to the equilibrium bond length of an isolated H₂ molecule (0.74 Å). In contrast, H₂ adsorbs strongly on Pt-decorated ZnO, as indicated by binding energies on the Pt site of -1.47 eV and -1.62 eV on the O-t₁ and Zn-t₁ surfaces, respectively, along with spontaneous dissociation postadsorption (H–H bond distances of 1.74 to 2.42 Å; see Figure 5b,c). Upon dissociation, the atomic H forms bonds with the Pt atoms at bond lengths ranging from 1.6 to 1.7 Å, with Figure 5b illustrating the spontaneous dissociation of H₂ on the Pt cluster during a DFT structure relaxation calculation. Thus, we expect Pt decoration to significantly facilitate both H₂ adsorption and H₂ dissociation on the ZnO surface, thereby enhancing the reactivity of hydrogen with available oxygen and reducing any kinetic barriers associated with H₂ dissociation.

2.3. LOD, Selectivity, Response, Recovery, and Stability. To evaluate the lower detection limit of the 2 s Pt-deposited sensor (at 225 °C), we measured the response over a range of low hydrogen concentrations, from 5 to 0.1

ppm. The dynamical response of the sensor, plotted as measured current, is displayed in Figure 6a and demonstrates a strong response of ~185% at 5 ppm hydrogen. Importantly, the sensor yields a measurable 38% response at an extremely low hydrogen concentration of 0.1 ppm, which we identify as the limit of detection (LOD), highlighting the ability of the sensor to detect hydrogen leaks early and fast, even under low (or trace) concentrations. Also, we observe marginal hysteresis in the dynamical response as hydrogen gas concentration is increased and decreased (Figure 6a), which may be attributed to differences in adsorption and desorption kinetics. Similarly, low levels of hysteresis are observed for the Pt nanocluster-decorated sample even across larger ranges of hydrogen concentrations (1000 to 10k ppm and vice versa; see Figure S4a). Thus, the Pt nanocluster-decorated ZnO thin film is a promising framework for hydrogen sensing as it combines a swift and reversible response with an extremely low LOD.

The response and recovery characteristics of the sensor, as depicted in panels b and c of Figure 6, provide critical insights into its dynamic performance when exposed to hydrogen. The response time (t_{res}) is defined as the duration needed for the sensor to achieve 90% of its maximum current after exposure to hydrogen gas, which reflects the sensor's ability to quickly

detect changes in the target gas concentration. The recovery time (t_{rec}) is the time the sensor takes to return to 90% of its baseline current after hydrogen is removed and synthetic air is introduced. As shown in **Figure 6**, the Pt-decorated ZnO (with 2 s deposition time) sensor exhibits significantly faster response and recovery times ($t_{res} = 10$ s, $t_{rec} = 3$ s, **Figure 6c**) compared to pristine ZnO ($t_{res} = 45$ s, $t_{rec} = 22$ s, **Figure 6b**) for 10k ppm of hydrogen concentration, highlighting the enhanced kinetics of adsorption and desorption provided by Pt decoration. Thus, we confirm that Pt nanocluster decoration of ZnO significantly improves t_{res} and t_{rec} compared to pristine ZnO, showcasing the critical role of Pt in enhancing the sensor's performance. Selectivity is a crucial parameter for gas sensors, as it defines their ability to specifically detect a target gas in the presence of other ambient gases. To evaluate selectivity, we tested pristine and Pt nanocluster-decorated (2 s Pt deposition) ZnO sensors with various gases at a concentration of 5 ppm under identical measurement conditions, including operating temperature. Pt nanocluster-decorated ZnO sensors demonstrated higher selectivity for hydrogen over other gases, such as CO, ammonia, ethylene, methane, NO₂, and acetone, as quantified by the higher response shown toward hydrogen in **Figure 6d**. For clarity, the quantitative sensor responses toward various interfering gases are summarized in **Table S4**, which further confirms the high selectivity of the sensor toward hydrogen. The incorporation of Pt onto ZnO enhances the catalytic activity of the sensor surface by favoring the adsorption and dissociation of hydrogen molecules (**Figure 5**). We observe enhanced selectivity of the Pt nanocluster-decorated ZnO sensor toward hydrogen compared to pristine ZnO, as shown in **Figure 6d**.

The repeatability of the sensor response in detecting hydrogen at a 1% concentration was assessed across multiple cycles for both pristine and Pt nanocluster-decorated (2 s deposition time) ZnO sensors. As quantified by the measured current in panels a and b of **Figure 7**, both pristine and Pt-decorated ZnO sensors exhibit consistent responses across cycles. Specifically, the Pt-decorated sensor shows a particularly consistent response (~51,765% to 52,987%, **Figure 7b**) compared to the pristine sample (~1,979% to 2,250%, **Figure 7a**). This consistency over multiple cycles indicates reliable sensor functionality with repeated hydrogen exposures, particularly for the Pt nanocluster-decorated sensor. The reproducibility of the sensors was verified by comparing the response across three independently fabricated samples in different batches. As shown in **Figure 7c**, the response variation across these sensors was minimal, indicating high reproducibility when they were exposed to different hydrogen concentrations. To evaluate long-term stability, we tracked the sensor response over several months for both the pristine (red symbols) and Pt-decorated (blue symbols) samples, as shown in **Figure 7d**. Notably, the Pt nanocluster-decorated ZnO sensor maintains a stable response after approximately 1 year of fabrication, which is likely due to the robust chemical and structural integrity of the Pt-ZnO interface. On the other hand, the response of pristine ZnO drops steadily with time after fabrication. Thus, the durability and long-term stability of the Pt nanocluster-decorated ZnO sensor's performance further underscore its potential for practical hydrogen detection.

In gas sensing applications, the work function is a key parameter that helps to understand the fundamental mechanisms of charge transfer and reaction kinetics. It directly

influences how a material interacts with gas molecules, as the adsorption and desorption of gases involve electron transfer processes that affect the material's surface potential.^{45,46} To investigate these mechanisms, we conducted Kelvin probe force microscopy (KPFM) measurements on both ZnO and Pt films to calculate their work function values. In this study, we derived the work function values of ZnO and Pt films using **eq S3** (see **Section S3**). We found the work function of ZnO to be approximately 4.5 eV, while that of Pt was 5.2 eV. Due to this difference in the work function values, electrons from the surface of ZnO will transfer to the Pt atoms until the Fermi levels of both materials equilibrate. The electron transfer can lead to the formation of a depletion region at the ZnO–Pt junction, where the semiconductor band edges bend "upward" with consequent impact on the sensor's electrical conductivity and response to gas exposure.

4. Gas Sensing Mechanism. We performed DFT-based calculations quantifying adsorption and reaction energetics on pristine and Pt nanocluster-decorated ZnO surfaces to unearth the gas sensing mechanism and the specific ZnO surface termination that contributes to our measured response, as well as to further understand the intrinsic response of ZnO and the role of Pt in hydrogen detection. Within the gas sensing literature of metal oxides, the widely accepted mechanism is the "adsorbed oxygen" model,^{47,48} where oxygen from the atmosphere gets adsorbed on the surface of the oxide sensor under ambient conditions. The adsorbed oxygen pulls out electrons from the metal oxide, thereby reducing the free electron concentration for an *n*-type semiconductor (or increasing the free hole concentration for a *p*-type semiconductor). When the oxide surface is subsequently exposed to H₂, the adsorbed oxygen reacts to form water, thereby releasing the electrons that were captured by the oxygen and causing an increase in the measured current for *n*-type semiconductors (or a decrease in current for *p*-type semiconductors). This change in measured current is the sensor's response to the gas' (hydrogen's) presence. Similar to forming H₂O, the adsorbed oxygen can also react with H₂ to form OH, in which case the number of electrons released back is fewer compared to H₂O formation causing a reduced change in measured current. However, there has been recent evidence of tangible sensor response to a target gas (such as H₂) in the absence of ambient oxygen, along with evidence of poor response in the presence of ambient oxygen,⁴⁹ thereby contesting the adsorbed oxygen model. In such cases, the sensor response can be attributed to the Mars-van Krevelen mechanism,^{50,51} where the target (H₂) gas plucks out one of the oxygen from the metal oxide lattice, leaving behind electrons that cause a change in the measured current. The lattice oxygen removed by the target gas can subsequently be replenished by atmospheric oxygen under ambient conditions (at elevated temperatures) after the target gas has been flushed out. Thus, it is important to identify the specific mechanism in our ZnO-based device to facilitate further improvements and optimization of performance.

The binding energies of various adsorbates, including atomic and molecular hydrogen, atomic and molecular oxygen, and H₂O on both the O-t₁ (panel a) and Zn-t₁ (panel b) surfaces of ZnO, are compiled in **Figure 8**. We considered four possible sites for the adsorption of all species, identical to **Figure 5a**, wherein the Pt site represents the adsorption or binding of species in the presence of the Pt cluster on the ZnO surface. On the pristine O-t₁ surface, we find atomic hydrogen to bind

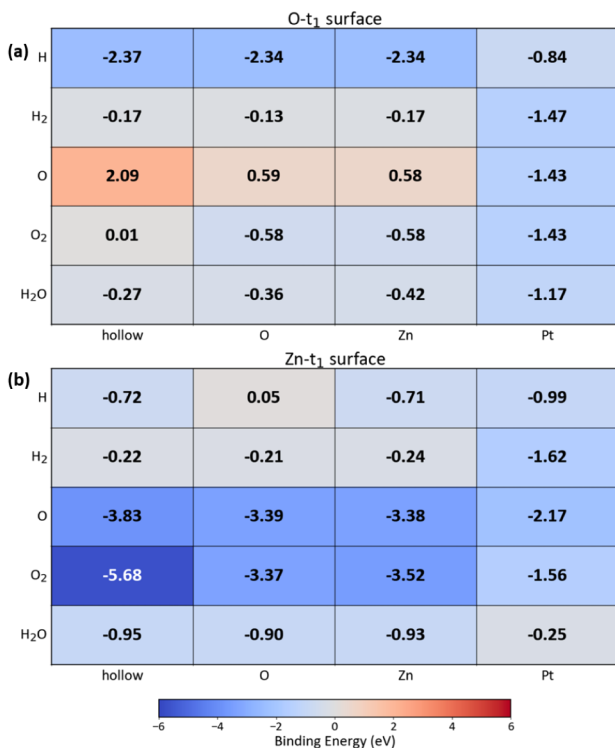


Figure 8. Heat map of binding energies of atomic H, molecular H₂, atomic O, molecular O₂, and molecular H₂O on the (a) O-t₁ and (b) Zn-t₁ surfaces. The hollow, O, Zn, and Pt correspond to possible sites for adsorption species, as defined in Figure 5.

strongly (~−2.37 to −2.34 eV) compared to molecular H₂ (~−0.17 to −0.13 eV) on all sites. Atomic hydrogen adsorption is also stronger on the O-t₁ surface than on the

Zn-t₁ surface (~−2.37 vs −0.72 eV). On the other hand, both atomic (−0.99 and −0.84 eV) and molecular (−1.62 and −1.47 eV) hydrogen bind strongly on the Pt site on both Zn-t₁ and O-t₁ surfaces, highlighting Pt's role as a facilitator of H₂ adsorption on the ZnO surface. Moreover, we observe spontaneous dissociation of molecular H₂ on the Pt site (see Figure 5b) to form atomic hydrogen, which can favor the reaction of hydrogen toward oxygen. Thus, the facilitation of molecular hydrogen adsorption and its dissociation to the reactive hydrogen form is one of the contributing factors to our observation of better sensor response on the Pt-decorated ZnO devices compared to the pristine ZnO sensors.

While molecular O₂ can adsorb on the O and Zn sites on O-t₁ (~−0.58 to 2.09 eV), atomic oxygen does not bind to the O-t₁ site (~0.58 to 2.09 eV), highlighting the nonspontaneity of oxygen dissociation on the O-t₁ surface. Thus, we do not expect the adsorbed oxygen pathway to be active on the O-t₁ surface in pristine ZnO. On the other hand, Pt decoration enables the adsorption of both molecular and atomic oxygen (−1.43 eV), indicating that Pt decoration can activate the adsorbed oxygen pathway on the O-t₁ surface, thereby possibly improving the sensing response. In the case of the Zn-t₁ surface, oxygen adsorption, both in molecular and atomic forms, is highly favored (binding energies below −3.3 eV), indicating that the adsorbed oxygen mechanism can be active on the pristine Zn-t₁ surface. Particularly, the O₂ molecule binds strongly at the hollow site on Zn-t₁ (−5.68 eV). The molecule dissociates, and each O atom occupies a hollow position on the surface to form three distinct bonds with nearby Zn atoms during a DFT structure relaxation. Pt decoration on Zn-t₁ increases the binding energies of both atomic and molecular oxygen (by a minimum of ~1.1 eV to a maximum of ~4 eV). However, Pt decoration does favor the binding of both atomic (−2.17 eV) and molecular (−1.56 eV)

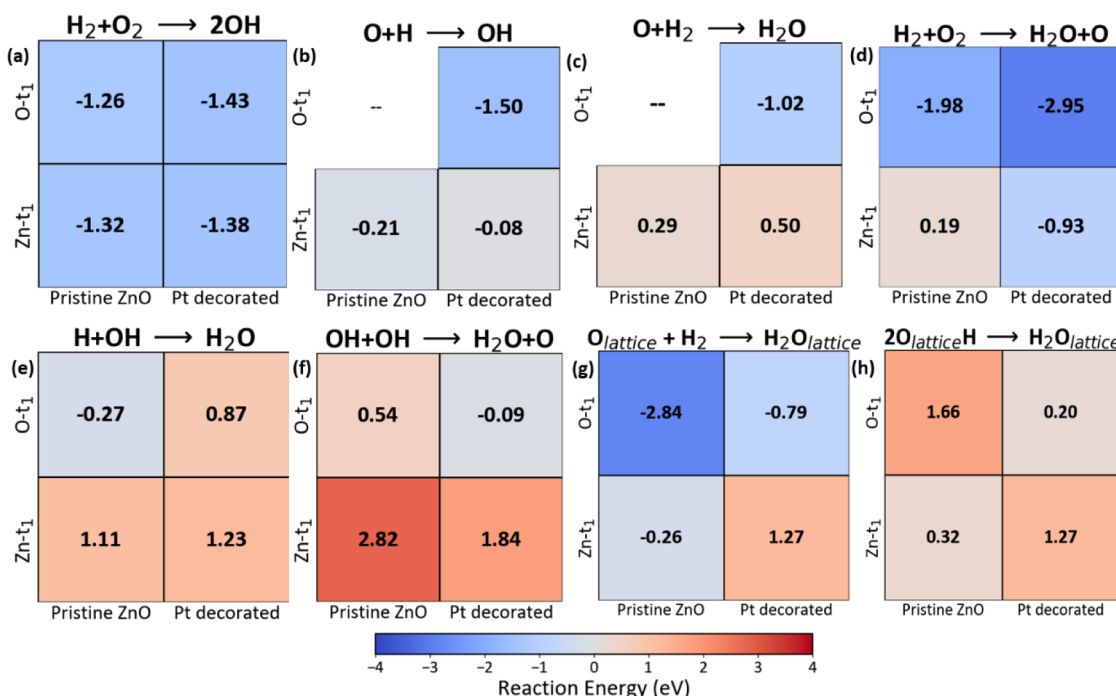


Figure 9. (a,b) OH formation energies from adsorbed oxygen and coadsorbed hydrogen in both molecular and atomic states, respectively. Water formation energies via (c,d) adsorbed oxygen and coadsorbed hydrogen pathway, (e,f) adsorbed OH with coadsorbed H or OH pathway, and (g,h) lattice oxygen pathway.

oxygen, thereby keeping the possibility of the adsorbed oxygen pathway active on the Zn-t₁ surface. Thus, we expect Pt decoration on ZnO to enable the adsorbed oxygen pathway on both the O-t₁ and Zn-t₁ terminations. Additionally, we expect water to bind reasonably well on both pristine (~ -0.27 to -0.95 eV) and Pt-decorated (~ -1.17 to -0.25 eV) O-t₁ and Zn-t₁ surfaces, indicating that water can exist as a stable adsorbed species on both surfaces. The H₂O molecule binds best with the subsurface Zn sites on the pristine O-t₁ surface (-0.42 eV), whereas it binds equally well at all sites on the pristine Zn-t₁ surface (-0.90 to -0.95 eV).

We evaluated the energies of various reaction pathways using DFT on both the O-t₁ and Zn-t₁ surfaces to evaluate the possible mechanisms active during device operation and compiled the results in **Figure 9**. Note that we did not consider transition or intermediate states of any reaction, focusing our efforts on the thermodynamic feasibility of possible reactions. We considered both H₂O and OH formation as possible products, given that both species can cause a change in the carrier concentration, thereby resulting in a sensor response. For calculating all reaction energies, we considered both reactants and products to be in their corresponding best binding sites (i.e., one of the hollow, O, or Zn sites in pristine ZnO, or at the Pt site for decorated ZnO).

In terms of OH formation, possible ways are through atomic O and H reactions and molecular O₂ and H₂ reactions (panels a and b in **Figure 9**; reaction energies in eV are normalized per OH formation), with both reactants and products being species that are adsorbed on one of the hollow, Zn, and O sites of pristine ZnO or on the Pt site of a Pt-decorated ZnO. Importantly, we find that OH formation is spontaneous (-1.50 eV) on the Pt-decorated O-t₁ surface considering formation from atomic species, while pristine O-t₁ cannot form OH from atomic O since the surface does not bind atomic O without Pt addition (see **Figure 8a**). OH formation is spontaneous on both pristine and Pt-decorated O-t₁ (-1.26 to -1.43 eV) when considering formation from molecular species. On the Zn-t₁ surface, OH formation is weakly favored (-0.08 to -0.21 eV) upon formation from atomic species, while OH formation is strongly favored from molecular species (-1.32 to -1.38 eV). The formation of OH from molecular reactants is more favored, likely due to O–H bonds being more stable than O–O or H–H bonds, which is also captured by the exothermic formation enthalpy of H₂O in the gas state from H₂ and O₂.^{52,53} Thus, we expect OH formation to be broadly favored in both pristine and Pt-decorated ZnO, with Pt decoration making a difference with respect to pristine ZnO only on the O-t₁ surface.

We calculated the reaction energies to form water (all energies in eV normalized per H₂O molecule) based on four sets of adsorbed reactants, namely, atomic O and molecular H₂, molecular O₂ and H₂, atomic H and adsorbed OH, and two adsorbed OH (via an “autoreduction” pathway), as displayed in panels c–f of **Figure 9**. Additionally, we considered water formation from the lattice oxygen (i.e., oxygen atoms that are intrinsic to the lattice and are not adsorbed species) via two mechanisms, namely, using molecular adsorbed hydrogen and atomic adsorbed hydrogen (panels g and h, **Figure 9**). Given that water formation from lattice oxygens requires the creation of a lattice oxygen vacancy (i.e., the hydrogen removes an oxygen from the lattice to form water), we have compiled the oxygen vacancy formation

energies on both the O-t₁ and Zn-t₁ surfaces, with and without Pt decoration (**Figure S7**). Post Pt addition, the oxygen vacancy formation energy of the lattice oxygens near the cluster increases for both terminations. For all reactions, we considered adsorbed O/O₂/OH to be at their best binding sites and adsorbed H/H₂ to be on a neighboring best binding site. For reactions where the reactant is not a stable adsorbed species (e.g., atomic O on pristine O-t₁; see **Figure 8**) we have not computed the reaction energies.

On the Zn-t₁ surface of pristine ZnO, we observe that water formation is not thermodynamically favored via all reaction pathways, with the exception of an adsorbed hydrogen molecule reacting with the lattice oxygen to form water (-0.26 eV, **Figure 9g**). With Pt decoration, water formation on Zn-t₁ is thermodynamically favored upon the reaction of molecular H₂ and molecular O₂ (-0.93 eV, **Figure 9d**), while the lattice oxygen pathway becomes unfavorable (1.27 eV, **Figure 9g**). Given that a reaction of molecular hydrogen with a lattice oxygen or coadsorbed molecular oxygen may require the formation of atomic hydrogen (or OH) as an intermediate species, we expect the occurrence of these reactions to be low. Hence, we expect the pristine or Pt-decorated Zn-t₁ surface to respond to the presence of hydrogen predominantly by forming adsorbed OH on the surface (panels a and b, **Figure 9**). However, the OH groups have strongly negative formation energies on the pristine Zn-t₁ surface and do not exhibit any favorable reaction energies toward water formation, indicating that the OH groups, once formed, will continue to remain on the Zn-t₁ surface. Such strong binding of OH groups may result in a drift in the response of the sensor (owing to the occupation of available active sites) and affect its stability over multiple cycles, which we do not observe in our experiments with pristine ZnO (**Figure 7d**). Thus, we expect the contributions of the Zn-t₁ surface to be minimal in the hydrogen sensor response observed with either pristine or Pt-decorated ZnO.

In the case of the O-t₁ surface, three reaction pathways are possible to form in pristine ZnO, namely, atomic H and adsorbed OH (-0.27 eV, **Figure 9e**), molecular H₂ and O₂ (-1.98 eV, **Figure 9d**), and molecular hydrogen with lattice oxygen (-2.84 eV, **Figure 9g**). On the other hand, Pt decoration enables water formation via the adsorbed OH autoreduction pathway (-0.09 eV, **Figure 9f**), disables the reaction of adsorbed H and OH (0.87 eV, **Figure 9e**), and allows water formation via molecular H₂ with molecular O₂ and molecular H₂ with lattice O. Thus, the key difference between pristine and Pt-decorated O-t₁ surfaces is the activation of the OH autoreduction pathway and the deactivation of the adsorbed H + OH pathway. Given that the occurrence of reactions with molecular H₂ or O₂ species can be limited (as discussed above in the Zn-t₁ case), we hypothesize that the sensor response of the O-t₁ surface is caused predominantly by the H + OH pathway in the pristine state and the OH autoreduction pathway in the Pt-decorated case, with the lattice oxygen pathway being active in both pristine and Pt-decorated ZnO.

We can expect the availability of OH species to be higher on the Pt-decorated O-t₁ surface compared to the pristine surface, since OH formation is favored through both adsorbed O + adsorbed H and molecular O₂ + molecular H₂ mechanisms in the Pt-decorated surface (panels a and b of **Figure 9**). Thus, the autoreduction of a higher concentration of OH groups on the Pt-decorated surface can result in a better sensor response

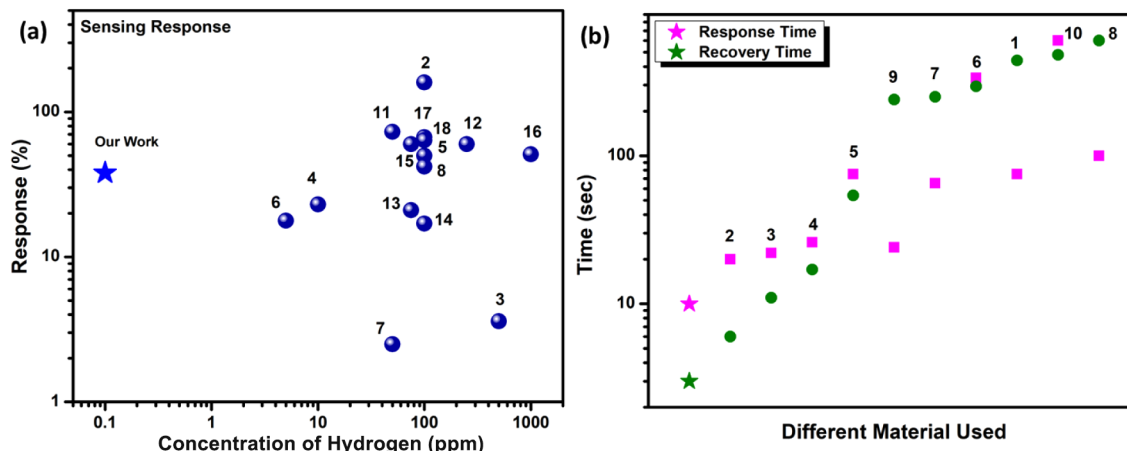


Figure 10. Comparison of our sensor with respect to literature data in terms of (a) the response at different hydrogen concentrations and (b) the response and recovery times.

compared to the $\text{H} + \text{OH}$ mechanism that is active on the pristine surface. Therefore, we hypothesize that the O-t_1 surface termination of ZnO predominantly contributes to our observed sensor response, with the adsorbed $\text{H} + \text{OH}$ mechanism and lattice oxygen pathway being more active on the pristine surface, while Pt decoration boosts the sensor response by facilitating the auto-reduction of OH groups adsorbed on the O-t_1 surface, alongside spontaneous adsorption and dissociation of molecular H_2 and keeping the lattice oxygen pathway active.

3. DISCUSSION

The performance of our Pt nanocluster-decorated ZnO sensor demonstrates high competitiveness in terms of its low LOD for hydrogen, along with exceptionally fast response and recovery times, which is important in ensuring the viability of a hydrogen-dominated sustainable energy economy. To clearly showcase the superior sensing performance of our devices, we conducted a benchmarking analysis by comparing our sensors' results with those from similar studies reported in the literature (Table S5).^{65–70} We summarize our benchmarking in Figure 10, where we plot the sensor's response as a function of its hydrogen LOD (which provides a visual comparison of sensitivity, panel a), and compare the response and recovery times of our sensor in real-time detection to other studies (panel b). Our *in situ* Pt-decorated ZnO -based sensor achieves the lowest LOD, detecting hydrogen at concentrations as low as 0.1 ppm (100 ppb), with a 38% sensing response, as shown in Figure 10a. Moreover, our sensor exhibits significantly faster response and recovery times—just 10 and 3 s, respectively—compared to similar gas sensors reported in the literature, as illustrated in Figure 10b. While several other sensors have been reported to detect ppb-level hydrogen, such sensors typically require higher operating temperatures compared to our Pt-decorated ZnO sensors. Also, our Pt-decorated sensor not only provides a low LOD for hydrogen but also a rapid response time compared to other devices, allowing it to detect low concentrations of hydrogen swiftly. Thus, we demonstrate the *in situ* Pt nanocluster-decorated ZnO sensor as a highly competitive and efficient candidate for hydrogen gas sensing, standing out due to its low LOD, rapid response and recovery time, and stability at moderate temperatures compared to sensors developed previously.

Typically, semiconducting metal oxides interact with a variety of gases, lacking inherent selectivity.^{6,54} However, the addition of platinum (Pt) to ZnO addresses these limitations by serving three important functions. First, Pt enhances the sensor's selectivity toward hydrogen (H_2). As illustrated in Figure 6d, cross-sensitivity tests demonstrate that, while pristine ZnO sensors respond to multiple gases, Pt nanocluster-decorated ZnO exhibits a markedly higher response to hydrogen compared to other gases. This pronounced increase in the hydrogen response ensures that hydrogen can be uniquely identified even in the presence of interfering gases. Second, Pt facilitates the efficient dissociation of H_2 molecules on its surface. Once H_2 dissociates at Pt sites, the resulting hydrogen radicals interact with surface-adsorbed oxygen or lattice oxygen species. This process, known as the spillover effect, is well-supported in the literature on noble metal-decorated oxide substrates.⁵⁵ Third, Pt enables the auto-reduction mechanism of OH groups on the ZnO surface, enabling them to form H_2O , which is normally easier to desorb than OH, thus increasing the stability of the sensor. Therefore, Pt not only enhances selectivity but also accelerates the reaction kinetics and enables essential reaction pathways for rapid sensor response and recovery.

Our reaction energy analysis of the lattice oxygen pathway, which we find to be active in both pristine and Pt nanocluster-decorated ZnO , aligns with earlier experimental observations on SnO_2 .^{49,50} Unlike previous studies, which have focused on the electronic structure changes with adsorption, our thermodynamic approach is in agreement with prior and current experimental data, emphasizing the often less-explored role of lattice oxygen in sensor operation. Thus, our findings support the contributions of the lattice oxygen pathway in addition to the typically cited adsorbed oxygen pathway. While our study provides valuable insights into the reaction mechanisms, it is important to acknowledge the limitations in our computational approach. The first is the inherent trade-off between accuracy and computational feasibility. Our calculations employed the generalized gradient approximation (GGA) as implemented in the Perdew–Burke–Ernzerhof (PBE)⁵⁶ functional. While GGA provides a reasonable balance between accuracy and computational cost, more sophisticated functionals like the strongly constrained and appropriately normed (SCAN)⁵⁷ can yield improved accuracy.⁵⁸ Due to the significant computational expense associated with SCAN and

the challenges in achieving convergence for our specific slab models, we opted for the computationally more tractable GGA. Future work may consider using SCAN or other meta-GGA functionals to improve the accuracy of binding and reaction energies.

We focused on the thermodynamics of reaction mechanisms at 0 K in this work, neglecting the kinetic effects. Although we expect the identified mechanisms to remain qualitatively valid at higher temperatures, the relative rates and overall selectivity could be influenced by the kinetic barriers. Additionally, we limited our calculations to the dominant (002) surface observed in XRD (Figure 3a) and we modeled the sputtered Pt using the smallest stable cluster, both of which are computational limitations of our study. Furthermore, we approximated the “on Pt” site as the only unique adsorption site on the cluster, neglecting potential edge effects at the Pt–ZnO interface. A more thorough investigation of the Pt–ZnO interface and a systematic exploration of various adsorption configurations, potentially using larger Pt clusters, could be useful in follow-up work. Despite these limitations, we believe that our work provides valuable mechanistic insights, offering a foundation for future experimental and theoretical work on sensors.

4. CONCLUSION

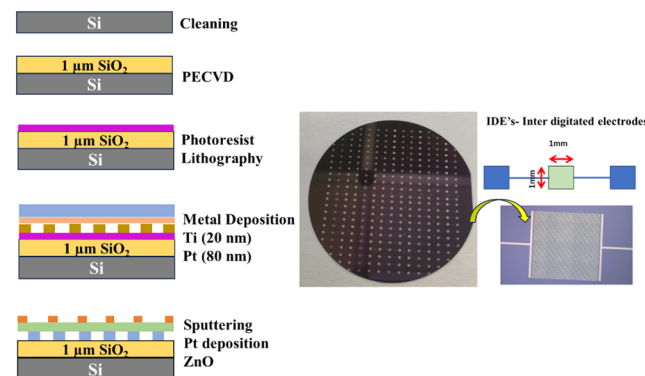
We have developed a Pt nanocluster-decorated ZnO thin-film sensor that delivers rapid response (10 s) and recovery (3 s) times at hydrogen concentrations of 10 000 ppm and detects hydrogen at levels as low as ~100 ppb. Utilizing an *in situ* sputtering technique followed by Pt nanocluster decoration, our sensor achieves stable and repeatable hydrogen detection. We confirmed the stability through 1 year of repeated hydrogen exposure and validated the reproducibility with three independently fabricated samples. Our fabrication method, which involves surface decoration without any postprocessing, is simple, scalable, and cost-effective for the large-scale production of hydrogen leak detection devices. This approach not only enhances sensing performance but also ensures the production of stable thin films with a reproducible synthesis process. Consequently, our Pt nanocluster-decorated ZnO sensor is well-suited for the large-scale production of efficient and reliable hydrogen sensing devices. In addition, the ability to detect trace hydrogen concentrations makes it useful for environmental monitoring and studying the impact of atmospheric hydrogen on the climate. Based on our DFT-based computations, we hypothesize that the O-exposed plane is the more active plane for sensing. The activation of multiple reaction pathways through Pt nanocluster decoration accounts for the substantial improvements in sensor performance, including increased sensitivity, reduced operating temperature, and faster response times. Our findings highlight the pivotal role of noble metal decoration, using scalable process techniques, in enhancing the performance of metal oxide sensors for practical applications in industrial and environmental monitoring systems. Apart from the results, we would also like to emphasize the approach of this study, which systematically combines experimental and computational investigations to elucidate possible reaction mechanisms apart from demonstrating repeatable and robust sensor performance under various experimental conditions. Such approaches will help advance the development of the next generation of metal-oxide-based sensors in a systematic and

accelerated fashion, which we hope the community will take up in future studies.

5. METHODS

5.1. Device Fabrication. An IDE system with uniform 5 μm spacing between electrodes was fabricated on a Si/SiO₂ substrate by using a two-step process involving optical lithography and sputtering. The IDE pattern was defined through lithography, followed by the deposition of a Ti/Pt (20 nm/80 nm) metal layer via DC magnetron sputtering. A liftoff process was then used to form contact pads. The sensing material, a metal oxide thin film, was subsequently deposited onto the IDE’s active region (1 mm² area) using radio frequency (RF) sputtering. The ZnO thin film was prepared through reactive RF magnetron sputtering from a high-purity (~99.99%) 3 in. ZnO target. Sputtering was conducted in a chamber maintained at 6.8e⁻³ mTorr, with a gas flow of 140 SCCM (standard cubic centimeters per minute) for chamber argon and 50 SCCM for magnetron argon, and the target-to-substrate distance was set at 7.5 cm. The chamber was evacuated to a base pressure of 3e⁻⁶ mTorr prior to initiating the sputtering process, with presputtering performed for approximately 1200 s (900 s with all gases and 300 s with the final parameters). A 40 nm thick ZnO layer was then deposited on the IDE using a hard shadow mask. To enhance sensing performance, the top surface of ZnO was decorated with Pt nanoclusters through sputtering at varying deposition times (1, 2, 4, and 6 s). The resulting sensor films were labeled as pristine ZnO, Pt_1s-ZnO, Pt_2s-ZnO, Pt_4s-ZnO, and Pt_6s-ZnO, respectively, corresponding to different Pt deposition times. The entire process flow is shown in Scheme 1. These sensor films were then subjected to further analysis and testing.

Scheme 1. Fabrication Process Flow of Pt Nanocluster-Decorated ZnO Film



5.2. Computational Details. We calculated the bulk, surface, and adsorption energetics of polar surfaces using spin-polarized DFT⁵⁹ as implemented in the Vienna ab initio simulation package (VASP).⁶⁰ Projector augmented wave⁶¹ (PAW) potentials were employed using a kinetic energy cutoff of 520 eV for the plane wave basis. We used a k -point density of 32 per Å to sample the reciprocal space (i.e., 32 subdivisions sampled along a unit reciprocal lattice vector). To approximate the electronic exchange and correlation, we used the PBE functional.⁵⁶ We utilized Grimme’s zero-damping DFT-D3⁶² dispersion correction in all calculations. During structural optimization, we converged the residual forces between atoms

to below $10.031\text{ eV}/\text{\AA}$ and the total energies to within $10^{-5}\text{ eV}/\text{cell}$. Dipole corrections were switched on during all relaxations. We have not explicitly corrected for the known oxygen molecule overbinding with GGA.⁶³ However, adding a correction to the O_2 molecule will not change any qualitative trends or conclusions of the study.

We used slab models, where each slab extends and is subject to periodic boundary conditions along the a and b axes, with the surface (s) lying perpendicular to the c -axis. We used 15 \AA thick slabs with 15 \AA of vacuum to separate periodic images along the c -axis. Slabs were created using the slab generator class of the Pymatgen package.⁶⁴ We used selective dynamics during structure relaxation, i.e., only the top two layers, along with any adsorbates, were allowed to relax, while all remaining layers were frozen to emulate bulk behavior. Details on cluster geometry and pseudo-hydrogen capping are provided in the Supporting Information.

ASSOCIATED CONTENT

Data Availability Statement

The computational data that support the findings of this study are openly available at our GitHub repository.

Supporting Information

The Supporting Information is available free of charge at <https://pubs.acs.org/doi/10.1021/acsanm.Sc04397>.

Details about the experimental and computational sections. It includes detailed descriptions of the experimental methods and materials characterizations. Additional data include supplementary tables that summarize crystallite size and strain (Table S1), elemental composition (Table S2), and oxygen species (Table S3); FESEM images (Figure S1); EPMA color map analysis (Figure S2); I – V characterization under various operating temperatures (Figure S3); and work function calculation by KPFM of Pt-decorated ZnO thin films (Section S3); sensing response hysteresis plot for the Pt-decorated ZnO sample and the linearity in the response of the sensor as a function of higher concentration (Figure S4); quantitative sensor response values toward different gases (Table S4); humidity effect (Figure S9); table for comparison of sensing performance with literature reports (Table S5). The computational section provides details of pseudo-molecule calculations, absolute surface energy calculations, and Pt cluster binding energetics (in Section S5), along with optimized structures and tabulated results to support the findings presented in the main manuscript (PDF)

AUTHOR INFORMATION

Corresponding Author

Navakanta Bhat – Centre for Nano Science and Engineering, Indian Institute of Science, Bengaluru 560012, India;  orcid.org/0000-0003-4364-1767; Email: navakant@iisc.ac.in, navakant@gmail.com

Authors

Puja Ghosh – Centre for Nano Science and Engineering, Indian Institute of Science, Bengaluru 560012, India;  orcid.org/0000-0003-0113-6383

Pritam Ghosh – Department of Materials Engineering, Indian Institute of Science, Bengaluru 560012, India

Rizwin Khanam – Centre for Nano Science and Engineering, Indian Institute of Science, Bengaluru 560012, India

Chandra Shekhar Prajapati – Indian Institute of Technology Patna, Patna, Bihar 801106, India

Aarti Nagarajan – Shell Global Solutions (US) Inc., Houston, Texas 77082, United States

Shreeja Das – Shell India Markets Pvt., Ltd., Bengaluru, Karnataka 562149, India

Rakesh Paleja – Shell Research Limited, London SE1 7NA, United Kingdom

Sharan Shetty – Shell India Markets Pvt., Ltd., Bengaluru, Karnataka 562149, India

Gopalakrishnan Sai Gautam – Department of Materials Engineering, Indian Institute of Science, Bengaluru 560012, India;  orcid.org/0000-0002-1303-0976

Complete contact information is available at:

<https://pubs.acs.org/10.1021/acsanm.Sc04397>

Author Contributions

The manuscript was written through the contributions of all authors. All authors have given their approval to the final version of the manuscript.

Notes

The authors declare no competing financial interest.

ACKNOWLEDGMENTS

The authors acknowledge financial support from Shell India Markets Private Limited. We acknowledge the technical support provided by the staff at the Micro and Nano Characterization Facility (MNCF) at the Centre for Nanoscience and Engineering (CeNSE) at the Indian Institute of Science (IISc), Bangalore, for the material characterization. The authors gratefully acknowledge the computational resources of the super computer ‘PARAM Pravega’ provided by Super Computer Education and Research Centre (SERC), IISc. The authors also acknowledge the computing resources provided to them on the high-performance computers noctua1 and noctua2 at the NHR Centre PC2. This was funded by the Federal Ministry of Education and Research (www.nhr-verein.de/unserer-partner).

REFERENCES

- (1) Pirrone, N.; Bella, F.; Hernández, S. Solar H₂ Production Systems: Current Status and Prospective Applications. *Green Chem.* **2022**, *24* (14), 5379–5402.
- (2) Aggarwal, P.; Sarkar, D.; Awasthi, K.; Menezes, P. W. Functional Role of Single-Atom Catalysts in Electrocatalytic Hydrogen Evolution: Current Developments and Future Challenges. *Coord. Chem. Rev.* **2022**, *452*, 214289.
- (3) Bryant, H. N.; Stevenson, D. S.; Heal, M. R.; Abraham, N. L. Impacts of hydrogen on tropospheric ozone and methane and their modulation by atmospheric NO_x. *Front. Energy Res.* **2024**, *12*, 12.
- (4) Ocko, I. B.; Hamburg, S. P. Climate consequences of hydrogen emissions. *Atmos. Chem. Phys.* **2022**, *22*, 9349–9368.
- (5) Nikolic, M. V.; Milovanovic, V.; Vasiljevic, Z. Z.; Stamenkovic, Z. Semiconductor Gas Sensors: Materials, Technology, Design, and Application. *Sensors* **2020**, *20* (22), 6694.
- (6) Ji, H.; Zeng, W.; Li, Y. Gas Sensing Mechanisms of Metal Oxide Semiconductors: A Focus Review. *Nanoscale* **2019**, *11* (47), 22664–22684.
- (7) Ghosh, P.; Roy, A.; Mukhopadhyay, S.; Narjinary, M.; Sundaram, S.; Sen, S.; Devi, P. S. A New Functional Composite for Photovoltaic and Sensor Applications. *Adv. Electron. Mater.* **2021**, *7* (3), 2000785.

- (8) Yuan, Z.; Li, J.; Meng, F. High Response N-Propanol Sensor Based on Co-Modified ZnO Nanorods. *J. Alloys Compd.* **2022**, *910*, 164971.
- (9) DMello, M. E.; Vishwanathan, S.; Bakuru, V. R.; Shanbhag, G. V.; Kalidindi, S. B. Metal–Organic Framework-Derived Co-Doped ZnO Nanostructures Anchored on N-Doped Carbon as a Room-Temperature Chemiresistive Hydrogen Sensor. *ACS Appl. Nano Mater.* **2023**, *6*, 238–247.
- (10) Nguyen, T. T. D.; Dao, D. V.; Lee, I. H.; Yu, Y. T.; Oh, S. Y. High response and selectivity toward hydrogen gas detection by In₂O₃ doped Pd@ZnO core-shell nanoparticles. *J. Alloys Compd.* **2021**, *854*, 157280.
- (11) Rajan, L.; Periasamy, C.; Sahula, V. Comprehensive Study on Electrical and Hydrogen Gas Sensing Characteristics of Pt/ZnO Nanocrystalline Thin Film-Based Schottky Diodes Grown on n-Si Substrate Using RF Sputtering. *IEEE Trans. Nanotechnol.* **2016**, *15* (2), 201–208.
- (12) Jeon, J.-Y.; Park, S.-J.; Ha, T.-J. Functionalization of Zinc Oxide Nanoflowers with Palladium Nanoparticles via Microwave Absorption for Room Temperature-Operating Hydrogen Gas Sensors in the Ppb Level. *ACS Appl. Mater. Interfaces* **2021**, *13* (21), 25082–25091.
- (13) Lupana, O.; Cretu, V.; Postica, V.; Ahmadi, M.; Cuanya, B. R.; Chow, L.; Tiginyanu, I.; Viana, B.; Pauporté, T.; Adelung, R. Silver-doped zinc oxide single nanowire multifunctional nanosensor with a significant enhancement in response. *Sens. Actuators, B* **2016**, *223*, 893–903.
- (14) Kashif, M.; Ali, M. E.; Ali, S. M. U.; Hashim, U. Sol–Gel Synthesis of Pd Doped ZnO Nanorods for Room Temperature Hydrogen Sensing Applications. *Ceram. Int.* **2013**, *39* (6), 6461–6466.
- (15) Rout, C. S.; Raju, A. R.; Govindaraj, A.; Rao, C. N. R. Hydrogen Sensors Based on ZnO Nanoparticles. *Solid State Commun.* **2006**, *138* (3), 136–138.
- (16) Kasapoğlu, A. E.; Habashyani, S.; Baltakesmez, A.; İskenderoğlu, D.; Gür, E. The Effect of the Change in the Amount of Sb Doping in ZnO Nanorods for Hydrogen Gas Sensors. *Int. J. Hydrogen Energy* **2021**, *46* (41), 21715–21725.
- (17) Hu, K.; Wang, F.; Yan, Y.; Liu, H.; Shen, Z. One Step from Nanofiber to Functional Hybrid Structure: Pd Doped ZnO/SnO₂ Heterojunction Nanofibers with Hexagonal ZnO Columns for Enhanced Low-Temperature Hydrogen Gas Sensing. *Ceram. Int.* **2021**, *47* (11), 15228–15236.
- (18) Lupan, O.; Postica, V.; Wolff, N.; Su, J.; Labat, F.; Ciofini, I.; Cavers, H.; Adelung, R.; Polonskyi, O.; Faupel, F.; Kienle, L.; Viana, B.; Pauporté, T. Low-Temperature Solution Synthesis of Au-Modified ZnO Nanowires for Highly Efficient Hydrogen Nanosensors. *ACS Appl. Mater. Interfaces* **2019**, *11* (35), 32115–32126.
- (19) Kim, J. H.; Mirzaei, A.; Osada, M.; Kim, H. W.; Kim, S. S. Hydrogen sensing characteristics of Pd-decorated ultrathin ZnO nanosheets. *Sens. Actuators, B* **2021**, *329*, 129222.
- (20) Xu, J.; Shun, Y.; Pan, Q.; Qin, J. Sensing Characteristics of Double Layer Film of ZnO. *Sens. Actuators, B* **2000**, *66* (1–3), 161–163.
- (21) Tamaekong, N.; Liewhiran, C.; Wisitsoraat, A.; Phanichphant, S. Sensing Characteristics of Flame-Spray-Made Pt/ZnO Thick Films as H₂ Gas Sensor. *Sensors* **2009**, *9* (9), 6652–6669.
- (22) Tien, L. C.; Sadik, P. W.; Norton, D. P.; Voss, L. F.; Pearton, S. J.; Wang, H. T.; Kang, B. S.; Ren, F.; Jun, J.; Lin, J. Hydrogen Sensing at Room Temperature with Pt-Coated ZnO Thin Films and Nanorods. *Appl. Phys. Lett.* **2005**, *87* (22), 222106.
- (23) Bhati, V. S.; Ranwa, S.; Fanetti, M.; Valant, M.; Kumar, M. Efficient Hydrogen Sensor Based on Ni-Doped ZnO Nanostructures by RF Sputtering. *Sens. Actuators, B* **2018**, *255*, 588–597.
- (24) Drmosh, Q. A.; Yamani, Z. H. Hydrogen Sensing Properties of Sputtered ZnO Films Decorated with Pt Nanoparticles. *Ceram. Int.* **2016**, *42* (10), 12378–12384.
- (25) Drmosh, Q. A.; Yamani, Z. H. S. Characterization, and Hydrogen Gas Sensing Properties of AuNs-Catalyzed ZnO Sputtered Thin Films. *Appl. Surf. Sci.* **2016**, *375*, 57–64.
- (26) Jiao, M.; Van Duy, N.; Chien, N. V.; Hoa, N. D.; Van Hieu, N.; Hjort, K.; Nguyen, H. On-Chip Growth of Patterned ZnO Nanorod Sensors with PdO Decoration for Enhancement of Hydrogen-Sensing Performance. *Int. J. Hydrogen Energy* **2017**, *42* (25), 16294–16304.
- (27) Kardeş, M.; Öztürk, K. A Comparative Investigation of Photocatalyst ZnO Nanorods Grown on Different Seed Layers: Influence of Annealing Temperature and Atmosphere. *Res. Chem. Intermed.* **2024**, *50* (1), 353–372.
- (28) Jain, N.; Kumawat, R.; Sharma, S. K. Effect of Substrate Temperature on the Microstructural and Optical Properties of RF Sputtered Grown ZnO Thin Films. *Mater. Today: proc.* **2020**, *30*, 93–99.
- (29) Karthick, K.; Srinivasan, D.; Christopher, J. B. Fabrication of highly c-axis Mg doped ZnO on c-cut sapphire substrate by rf sputtering for hydrogen sensing. *J. Mater. Sci.: Mater. Electron.* **2017**, *28*, 11979–11986.
- (30) Qin, N.; Xiang, Q.; Zhao, H.; Zhang, J.; Xu, J. Evolution of ZnO Microstructures from Hexagonal Disk to Prismoid, Prism and Pyramid and Their Crystal Facet-Dependent Gas Sensing Properties. *CrystEngcomm* **2014**, *16* (30), 7062–7073.
- (31) Ranwa, S.; Kulriya, P. K.; Sahu, V. K.; Kukreja, L. M.; Kumar, M. Defect-Free ZnO Nanorods for Low Temperature Hydrogen Sensor Applications. *Appl. Phys. Lett.* **2014**, *105* (21), 213103.
- (32) Hung, P.-S.; Chou, Y.-S.; Huang, B.-H.; Cheng, I.-K.; Wang, G.-R.; Chung, W.-A.; Pan, F.-M.; Wu, P.-W. A Vertically Integrated ZnO-Based Hydrogen Sensor with Hierarchical Bi-Layered Inverse Opals. *Sens. Actuators, B* **2020**, *325*, 128779.
- (33) Hassan, J. J.; Mahdi, M. A.; Chin, C. W.; Abu-Hassan, H.; Hassan, Z. Room Temperature Hydrogen Gas Sensor Based on ZnO Nanorod Arrays Grown on a SiO₂/Si Substrate via a Microwave-Assisted Chemical Solution Method. *J. Alloys Compd.* **2013**, *546*, 107–111.
- (34) Das, S. N.; Kar, J. P.; Choi, J.-H.; Lee, T. I.; Moon, K.-J.; Myoung, J.-M. Fabrication and Characterization of ZnO Single Nanowire-Based Hydrogen Sensor. *J. Phys. Chem. C* **2010**, *114* (3), 1689–1693.
- (35) Moll, N.; Kley, A.; Pehlke, E.; Scheffler, M. GaAs Equilibrium Crystal Shape from First Principles. *Phys. Rev. B* **1996**, *54* (12), 8844–8855.
- (36) Yufei, Z.; Zhiyou, G.; Xiaoqi, G.; Dongxing, C.; Yunxiao, D.; Hongtao, Z. First-Principles of Wurtzite ZnO (0001) and (0001̄) Surface Structures. *J. Semicond.* **2010**, *31* (8), 082001.
- (37) Yu, K.; Carter, E. A. A Strategy to Stabilize Kesterite CZTS for High-Performance Solar Cells. *Chem. Mater.* **2015**, *27* (8), 2920–2927.
- (38) Joshi, N.; da Silva, L. F.; Shimizu, F. M.; Mastelaro, V. R.; M'Peko, J. C.; Lin, L.; Oliveira, O. N. UV-Assisted Chemiresistors Made with Gold-Modified ZnO Nanorods to Detect Ozone Gas at Room Temperature. *Microchim. Acta* **2019**, *186* (7), 418.
- (39) Li, Z.; Yi, J. Drastically Enhanced Ammonia Sensing of Pt/ZnO Ordered Porous Ultra-Thin Films. *Sens. Actuators, B* **2020**, *317*, 128217.
- (40) Ghosh, P.; Manikandan, M.; Sen, S.; Devi, P. S. Some Interesting Insights into the Acetone Sensing Characteristics of Monoclinic WO₃. *Mater. Adv.* **2023**, *4* (4), 1146–1160.
- (41) Vijayakumar, Y.; Nagaraju, P.; Yaragani, V.; Parne, S. R.; Awwad, N. S.; Ramana Reddy, M. V. Nanostructured Al and Fe Co-Doped ZnO Thin Films for Enhanced Ammonia Detection. *Phys. B Condens. Matter* **2020**, *581*, 411976.
- (42) Hosseiniabadi, S.; Abrinaei, F.; Shirazi, M. Statistical and Fractal Features of Nanocrystalline AZO Thin Films. *Phys. Stat. Mech. Its Appl.* **2017**, *481*, 11–22.
- (43) Kumar, V.; Kawazoe, Y. Evolution of Atomic and Electronic Structure of Pt Clusters: Planar, Layered, Pyramidal, Cage, Cubic, and Octahedral Growth. *Phys. Rev. B* **2008**, *77* (20), 205418.
- (44) Xiao, L.; Wang, L. Structures of Platinum Clusters: Planar or Spherical? *J. Phys. Chem. A* **2004**, *108* (41), 8605–8614.
- (45) Mokrushin, A. S.; Nagornov, I. A.; Simonenko, T. L.; Simonenko, N. P.; Yu, G.; Khamova, T. V.; Kopitsa, G. P.;

- Evzrevoz, A. N.; Simonenko, E. P.; Sevastyanov, V. G.; et al. Chemoresistive Gas-Sensitive ZnO/Pt Nanocomposites Films Applied by Microplotter Printing with Increased Sensitivity to Benzene and Hydrogen. *Mater. Sci. Eng., B* **2021**, *271*, 115233.
- (46) Li, G.; Sun, Z.; Zhang, D.; Xu, Q.; Meng, L.; Qin, Y. Mechanism of Sensitivity Enhancement of a ZnO Nanofilm Gas Sensor by UV Light Illumination. *ACS Sens.* **2019**, *4* (6), 1577–1585.
- (47) Nadargi, D. Y.; Umar, A.; Nadargi, J. D.; Lokare, S. A.; Akbar, S.; Mulla, I. S.; Suryavanshi, S. S.; Bhandari, N. L.; Chaskar, M. G. Gas Sensors and Factors Influencing Sensing Mechanism with a Special Focus on MOS Sensors. *J. Mater. Sci.* **2023**, *58* (2), 559–582.
- (48) Ren, Q.; Cao, Y.-Q.; Arulraj, D.; Liu, C.; Wu, D.; Li, W.-M.; Li, A.-D. Review-Resistive-Type Hydrogen Sensors Based on Zinc Oxide Nanostructures. *J. Electrochem. Soc.* **2020**, *167* (6), 067528.
- (49) Zhu, L.; Zeng, W.; Li, Y. A Non-Oxygen Adsorption Mechanism for Hydrogen Detection of Nanostructured SnO₂ Based Sensors. *Mater. Res. Bull.* **2019**, *109*, 108–116.
- (50) Li, J.; Si, W.; Shi, L.; Gao, R.; Li, Q.; An, W.; Zhao, Z.; Zhang, L.; Bai, N.; Zou, X.; Li, G.-D. Essential Role of Lattice Oxygen in Hydrogen Sensing Reaction. *Nat. Commun.* **2024**, *15* (1), 2998.
- (51) Doornkamp, C.; Ponec, V. The Universal Character of the Mars and Van Krevelen Mechanism. *J. Mol. Catal. Chem.* **2000**, *162* (1), 19–32.
- (52) Chase, M. W. NIST-JANAF Thermochemical Tables, Fourth Edition. *J. Phys. Chem. Ref. Data* **1998**, *9*, 1–1951.
- (53) Cox, J. D.; Wagman, D. D.; Medvedev, V. A. CODATA Key Values for Thermodynamics; Hemisphere Pub. Corp., 1984; p 1.
- (54) Koo, W.-T.; Cho, H.-J.; Kim, D.-H.; Kim, Y. H.; Shin, H.; Penner, R. M.; Kim, I.-D. Chemiresistive Hydrogen Sensors: Fundamentals, Recent Advances, and Challenges. *ACS Nano* **2020**, *14* (11), 14284–14322.
- (55) Prins, R. H. S. Facts and Fiction. *Chem. Rev.* **2012**, *112* (5), 2714–2738.
- (56) Perdew, J. P.; Burke, K.; Ernzerhof, M. Generalized Gradient Approximation Made Simple. *Phys. Rev. Lett.* **1996**, *77* (18), 3865–3868.
- (57) Sun, J.; Ruzsinszky, A.; Perdew, J. P. Strongly Constrained and Appropriately Normed Semilocal Density Functional. *Phys. Rev. Lett.* **2015**, *115* (3), 036402.
- (58) Sai Gautam, G.; Carter, E. A. Evaluating Transition Metal Oxides within DFT-SCAN and \$text{SCAN}+U\$ Frameworks for Solar Thermochemical Applications. *Phys. Rev. Mater.* **2018**, *2* (9), 095401.
- (59) Hohenberg, P.; Kohn, W. Inhomogeneous Electron Gas. *Phys. Rev.* **1964**, *136* (3B), B864–B871.
- (60) Kresse, G.; Furthmüller, J. Efficient Iterative Schemes for Ab Initio Total-Energy Calculations Using a Plane-Wave Basis Set. *Phys. Rev. B* **1996**, *54* (16), 11169–11186.
- (61) Kresse, G.; Joubert, D. From Ultrasoft Pseudopotentials to the Projector Augmented-Wave Method. *Phys. Rev. B* **1999**, *59* (3), 1758–1775.
- (62) Grimme, S.; Antony, J.; Ehrlich, S.; Krieg, H. A Consistent and Accurate *Ab Initio* Parametrization of Density Functional Dispersion Correction (DFT-D) for the 94 Elements H-Pu. *J. Chem. Phys.* **2010**, *132* (15), 154104.
- (63) Wang, L.; Maxisch, T.; Ceder, G. Oxidation Energies of Transition Metal Oxides within the \$\mathit{GGA}+\mathit{U}\$ Framework. *Phys. Rev. B* **2006**, *73* (19), 195107.
- (64) Ong, S. P.; Richards, W. D.; Jain, A.; Hautier, G.; Kocher, M.; Cholia, S.; Gunter, D.; Chevrier, V. L.; Persson, K. A.; Ceder, G. Python Materials Genomics (Pymatgen): A Robust, Open-Source Python Library for Materials Analysis. *Comput. Mater. Sci.* **2013**, *68*, 314–319.
- (65) Sanjana Devi, V.S.; Balraj, B.; Siva, C.; Amuthameena, S. Synthesis of nitrogen-doped zinc oxide nanomaterials for hydrogen gas sensing applications. *J. Mater. Sci.: Mater. Electron.* **2023**, *34*, 1905.
- (66) Al-Asedy, H. J.; Bidin, N.; Al-Khafaji, S. A.; Bakhtiar, H. Sol-gel grown aluminum/gallium co-doped ZnO nanostructures: Hydrogen gas sensing attributes. *Mater. Sci. Semicond. Process.* **2018**, *77*, 50–57.
- (67) Hosseinejad, M. T.; Ghoranneviss, M.; Hantehzadeh, M. R.; Darabi, E. Characterization and hydrogen gas sensing performance of Al-doped ZnO thin films synthesized by low energy plasma focus device. *J. Alloys Compd.* **2016**, *689*, 740–750.
- (68) Malik, R. K.; Khanna, R.; Sharma, G. L.; Pavunny, S. P.; Katiyar, R. S. Hydrogen Sensing Properties of Copper-Doped Zinc Oxide Thin Films. *IEEE Sens. J.* **2015**, *15*, 7021–7028.
- (69) Hsiao, Y. J.; Nagarjuna, Y.; Huang, G. Y.; Lin, M. Preparation of tungsten-doped zinc oxide thin films by co-sputtering for micro-gas sensing devices. *J. Alloys Compd.* **2023**, *960*, 170567.
- (70) Bhati, V. S.; Ranwa, S.; Rajamani, S.; Kumari, K.; Raliya, R.; Biswas, P.; Kumar, M. Improved Sensitivity with Low Limit of Detection of a Hydrogen Gas Sensor Based on rGO-Loaded Ni-Doped ZnO Nanostructures. *ACS Appl. Mater. Interfaces* **2018**, *10*, 11116–11124.



CAS BIOFINDER DISCOVERY PLATFORM™

STOP DIGGING THROUGH DATA — START MAKING DISCOVERIES

CAS BioFinder helps you find the right biological insights in seconds

Start your search

